Space Science Reviews (2025) 221:38
https://doi.org/10.1007/s11214-025-01162-w

SPECIAL COMMUNICATION

The Negative Ions at the Lunar Surface (NILS) Instrument on the Chang'E-6 Mission

Romain Canu-Blot[1,2] · Martin Wieser[1] · Maté Kérényi[1] · Stas Barabash[1] · Xiao-Dong Wang[1] · Thomas Maynadié[1] · Aibing Zhang[3,4] · Wenjing Wang[3] · Neil Melville[5] · Qiong Wang[6] · Yongliao Zou[3] · Hao Dou[6] · Hanyou Zhu[6] · Vesa Alatalo[1] · Andreas Edström[1] · Leif Kalla[1] · Stefan Karlsson[1] · Magnus Oja[1] · Jonas Olsen[1] · Joakim Peterson[1] · Daniel Stålnacke[1] · David Upton[1]

Received: 26 June 2024 / Accepted: 19 March 2025 / Published online: 14 April 2025

Abstract
The Negative Ions at the Lunar Surface (NILS) instrument is a compact mass resolving negative ion and electron analyser flown on the Chinese Chang'E-6 mission to the Moon. NILS measures negative ions and electrons in the energy range of 3 eV/q to 3 keV/q with a mass resolution $m/\Delta m$ of about 2. The mass resolution is sufficient to separate charge-converted solar wind protons and sputtered negatively charged atoms form the surface. An electro-magnetic electron suppression system allows to switch between electron and ion measurements. The fan-shaped field of view is divided into 16 discrete angular pixels that are scanned sequentially. For each viewing direction, an electron and an ion energy spectrum is acquired in 4.06 s. NILS has a mass of 919 g, excluding cables and multi-layer insulation. Power consumption is on average 2.7 W during nominal operations.

Keywords Mass resolving negative ion analyzer · Geometric factor determination · Lunar surface · Solar wind - regolith interaction · Chang'E-6

Note by the Editor: This is a Special Communication. In addition to invited review papers and topical collections, Space Science Reviews publishes unsolicited Special Communications. These are papers linked to an earlier topical volume/collection, report-type papers, or timely papers dealing with a strong space-science-technology combination (such papers summarize the science and technology of an instrument or mission in one paper).

✉ R. Canu-Blot
romain.canu-blot@irf.se

1 Swedish Institute of Space Physics, Bengt Hultqvists väg 1, Kiruna, 98192, Sweden

2 Department of Physics, Umeå University, 907 36 Umeå, Sweden

3 National Space Science Center (NSSC), Chinese Academy of Sciences (CAS), No. 1 Nanertiao, Zhongguancun, Haidian district, Beijing, 100190, China

4 University of Chinese Academy of Sciences, No.19(A) Yuquan Road, Shijingshan district, Beijing, 100049, China

5 European Space Agency/European Space Research and Technology Centre, Keplerlaan 1, Noordwijk, 2201AZ, The Netherlands

6 Lunar Exploration and Space Engineering Center (LESEC), Beijing, 100043, China

Symbols

α	Azimuths viewing angle (deg)
θ	Elevation viewing angle (deg)
$\mathcal{D}$	Beam energy (per charge) distribution function (q/eV)
γ	Particle species defining a mass and charge
f	Particle phase space density function (s^3/m^6)
$\mathbf{x}$	Position vector in position space (m)
$\mathbf{v}$	Position vector in velocity space (m/s)
$\mathcal{R}$	Instrument response function
$\mathcal{R}_0$	Ideal instrument response function
$\mathbf{u}$	Measurement setting (m/s)
ξ	Absolute energy per charge (eV/q)
e	Elementary charge (C)
q	Charge state
$\mathcal{C}$	Number of counts observed by the instrument
τ	Instrument time resolution (s)
$\mathbf{A}$	Instrument effective area (m^2)
κ	Scaling factor converting both instrument energy/angular response probability density functions to the instrument response probability function ($sr \cdot eV/q$)
$\mathcal{R}_\Omega$	Instrument angular response function (sr^{-1})
$\mathcal{R}_E$	Instrument energy response function (q/eV)
ξ_u	Average absolute energy per charge for a measurement $\mathbf{u}$ (eV/q)
$\mathcal{K}$	Electrostatic analyser constant
E_{res}	Energy resolution (eV/eV)
θ_u	Average elevation viewing angle for a measurement $\mathbf{u}$ (deg)
α_u	Average azimuths viewing angle for a measurement $\mathbf{u}$ (deg)
Γ	Angular analyser constant
θ_u^*	Average elevation viewing angle (for a measurement $\mathbf{u}$) corrected for the energy dependence (deg)
$\mathcal{T}$	Electron transmission efficiency
η	Average detection probability
$\mathcal{GF}$	Instrument geometric factor, velocity definition ($cm^2 \cdot sr \cdot eV/eV$)
$\mathcal{GF}_0$	Instrument absolute geometric factor, velocity definition ($cm^2 \cdot sr \cdot eV/eV$)
n_B	Particle number density (m^{-3})
j	Current density (A/m^2)
I_{prim}	Positive ion current entering the NIOS (A)
Φ	Particle number flux ($\#/\left(m^2 \cdot s\right)$)
Ω	Solid angle (sr)
$\mathcal{GF}_0^{\text{gem}}$	Instrument absolute geometric factor, velocity definition, derived from the instrument geometry only ($cm^2 \cdot sr \cdot eV/eV$)
$\mathbb{GF}$	Instrument geometric factor, energy definition ($cm^2 \cdot sr \cdot eV/eV$)
J	Particle differential number flux ($(cm^2 \cdot s \cdot sr \cdot eV)^{-1}$)

1 Introduction

1.1 An Elusive Species

Almost all visible matter in the universe is in the form of a plasma consisting of positively charged ions and negatively charged electrons. The plasma may also contain negatively

charged ions, but only a few and often indirect observations of negative ions beyond the Earth have been reported. Negative ions have been inferred to be present in the solar photosphere (Chandrasekhar and Münch 1946). Negative molecular ions have been found in the interstellar medium and evolved stars using radio observations (Millar et al. 2017). Negative ions have also been observed in-situ in the terrestrial ionosphere by negative ion instruments (e.g., Arnold and Krankowsky 1971), but no dedicated negative ion instrument has flown beyond Earth. Nevertheless, negative ion populations have been found as anomalous signals in electron data at Comet 1P/Halley (Chaizy et al. 1991), Titan (Coates et al. 2007), icy moons of Saturn (Coates et al. 2010; Teolis et al. 2010; Desai et al. 2018), Comet 67P (Burch et al. 2015), and the upper atmosphere of Mars (Halekas et al. 2015). 'Negative ionospheres' should exist to some extent at any planetary object.

1.2 The Moon as Laboratory

When solar wind ions interact directly with planetary surfaces, they may be backscattered from the surface or they may result in sputtering of surface atoms. The Moon is an ideal laboratory for studying these interactions and so far most in-situ observations of these processes have been done at the Moon. Although most of the particles that are emitted due to solar wind precipitation are electrically neutral, both positive and negative charge states are possible. Both positive and neutral charge fractions have been observed from orbiting spacecraft, for example H^+ (Saito et al. 2008; Tanaka et al. 2009; Lue et al. 2011), energetic H^0 (Wieser et al. 2009; McComas et al. 2009) or energetic He^0 and O^0 (Vorburger et al. 2014). Solar wind precipitation also causes sputtering of surface material (Yokota et al. 2009; Tanaka et al. 2009; Vorburger et al. 2014).

The further study of the neutral and positive fractions is currently an ongoing activity of the Advanced Small Analyzer for Neutrals (ASAN) on the Chinese National Space Agency's (CNSA) Chang'E-4 rover Yutu-2 on the lunar surface (Wieser et al. 2020, 2024). No unambiguous detection of negative ions has been done in the near-Moon environment so far. Negative ions are typically short-lived in space. They are weakly bound systems; for example, the extra electron in H^- has a binding energy of only 0.7 eV and is easily detached. At one astronomical unit (au) from the Sun, H^- has a lifetime of 70 ms against photo-detachment (Desai et al. 2021). Because of that, negative ion populations in general only exist close to the negative ion source. The importance of the negative ion population to the near-surface plasma environment is unclear and there are only coarse estimates of negative ion densities near exposed surfaces (e.g., Wekhof 1981). Due to the limited lifetime, the propagation distances of negative ions on the Moon are expected to be much shorter than the typical orbital altitudes of $\approx$100 km. This may explain why negative ions have not been detected by electron spectrometers on orbiters so far. Additionally, any negative ion signature from an electron spectrometer may be drowned out by the electron signal itself.

The lunar negative ion density estimates from Wekhof (1981) are shown in Fig. 1. In this model, the dominant negative ion species is H^-. An estimate of the negative hydrogen flux originating from solar wind backscattering from the surface can be made assuming that roughly the same fraction of solar wind protons impinging onto the surface are backscattered as negative ions and as positive ions. Similar charge-state fractions have been observed in the laboratory when protons scatter from oxide surfaces (Wieser et al. 2002; Jans et al. 2001). Figure 2 shows the negative hydrogen flux estimated in this way using the observed flux of backscattered protons from the Moon (Lue et al. 2014).

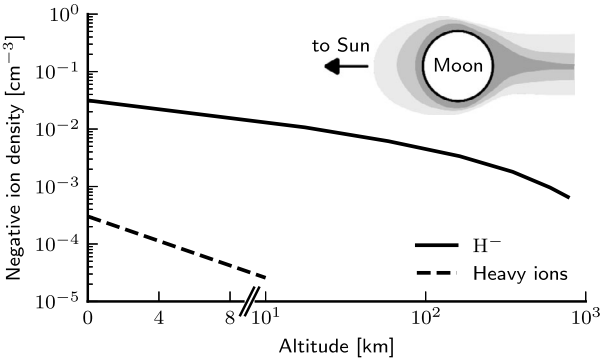

Fig. 1 Predicted anion-sphere around the Moon. H^- originating from solar wind H^+ dominates but a small sputtered population of heavier negative ions should also exist. Figure adapted from Wekhof (1981)

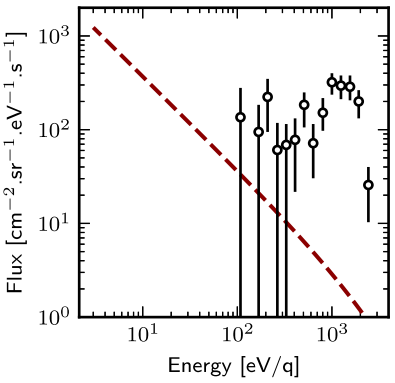

Fig. 2 Negative ion flux model (filled circles) based on measurements of protons back-scattered from the lunar surface (Lue et al. 2014) with the assumption that the positive and negative charge states are equally likely after interaction with the surface. The NILS one-count detection limit after 60 minutes of integration is shown as dotted line

1.3 Measuring Negative Ions at the Moon

The Negative Ions at the Lunar Surface (NILS) instrument is the first instrument to measure the negative ion flux on the lunar surface. NILS is an energy and mass resolving negative ion mass analyser based on the *SWIM family* of instruments (Wieser and Barabash 2016; Wieser et al. 2020). NILS (Fig. 3) is one of the international payloads on the lander of the Chang'E-6 lunar sample return mission (Zeng et al. 2023). NILS will establish whether the negative ion populations on the lunar surface predicted by Wekhof (1981) exist in the first place, and will provide context to previous indirect observations of negative ions in space. As the NILS measurements are made very close to the surface, the short lifetime of H^- does not significantly reduce the observed flux. Assuming that an equal amount of negative and positive hydrogen ions is emitted from the surface, for a nominal integration time of 60 minutes, the predicted signal at 1 keV would be almost two orders of magnitude above the NILS detection limit (Fig. 2).

1.4 NILS Science Objectives

NILS was designed to perform discovery-type measurements of the negative ion population on the lunar surface. NILS will address the following science questions:

1. How important are negative ions for space-surface interactions and environments of planetary bodies with surface-bound exospheres? Although positive ions resulting from

Fig. 3 NILS mission poster emphasising the collaborative exploration of the lunar environment. Artist: Jule Goerke (https://julegoerke.de)

plasma surface interaction are known to be a source for certain particle populations (e.g., Nishino et al. 2009), the fate of a possible negative ion population is not known. Negative ions could be a source for the tenuous lunar exosphere, a source mechanism that could also be applicable for other planetary bodies with surface-bound exospheres.

2. Do negative ions significantly contribute to and affect the lunar plasma environment? Despite the limited lifetime of negative ions, their contribution to the dynamics of the near-lunar surface plasma environment could be significant, but no constraining measurements exist.
3. Do negative ions constitute a substantial loss path for lunar surface elements? Both micrometeorite vaporisation and solar wind sputtering are a loss path for surface elements to the lunar exosphere. Depending on the element, near the surface negative ions could constitute a significant fraction of the emitted particles.

With NILS mounted on the lander section of the Chang'E-6 spacecraft, the time available for data taking for NILS is limited by the time needed for the lander to collect surface materials. NILS data collection will start shortly after landing and continue as long as thermal conditions permit until the launch of the return module containing the samples. After launch of the return capsule, the lander is turned off, and latest at that moment any data taking by NILS will stop. During its active time on the surface, NILS will establish how large the fraction of negative ions is in the scattered and sputtered particles from the lunar regolith and how this fraction depends on the energy and species of the particles. We will rely on measurements of upstream solar wind conditions from the electrostatic analyzer instrument (McFadden et al. 2008, ESA) on the Artemis-P1/P2 spacecrafts (Angelopoulos 2011) in lunar orbit. Since the observation of negative ions is highly exploratory and the mission time on the surface is limited, we formulate three different success levels for the actual measurements:

Threshold: Detect and quantify the presence or establish the upper limit flux of negative ions emitted from the lunar surface.

Nominal: Separate the energy distributions of scattered H^- and sputtered lunar negative ions and coarsely resolve the mass distribution of the observed negative ions for mass groups containing H^-, O^- and Al^-/Si^-.

Extended: Resolve the energy distributions for each species or mass group separately.

The threshold level of success can be reached with a total data collection time of one hour. Any longer operation time may make it possible to reach the nominal or even the extended levels. The way science questions are translated into measurement and performance requirements is shown in Table 1.

2 Instrument Description

2.1 Principle of Operation

The NILS instrument (Fig. 4) is a single-pixel negative ion mass analyzer with coarse mass resolution. Its single angular pixel can be electro-statically scanned across a fan-shaped field of view. The mass of the detected particles is determined by combining energy information from the electrostatic analyser with a particle velocity measurement in a time-of-flight cell. An electromagnet generates a variable magnetic field across the entrance aperture to either accept or reject electrons. This allows to alternatively measure a mass-resolved negative ion energy spectrum or the electron energy spectrum.

2.2 Functional Blocks

The NILS instrument consists of three different mechanically connected units: the sensor head, which includes a spring-loaded protective door; the electronic box; and a thermal radiator. NILS is thermally insulated to the spacecraft. NILS is a derivative of the *SWIM family* of instruments (Wieser and Barabash 2016) and is most similar to the Advanced Small Analyzer of Neutrals instrument (Wieser et al. 2020, ASAN). An overview of the functional blocks of the NILS instrument is shown in Fig. 5.

The ion-optical part of the sensor (Canu-Blot 2024, Sect. 3.3) can be divided into four functional blocks, all enclosed within the sensor head (see Fig. 6 and Fig. 7). An elevation scanning system used to select the instrument viewing direction, a magnetic electron suppression system, an electrostatic analyser for energy filtering, and a time-of-flight section for velocity measurement.

2.2.1 Elevation Scanning System

The elevation scanning system is used to control the viewing direction of the single angular pixel of the instrument. The system is a copy of the Solar Wind Monitor instrument (SWIM) flown on Chandrayaan-1 (Barabash et al. 2009). It consists of two cylindrical electrodes combined with a planar grid. Positive voltages are applied to the electrodes to obtain the desired viewing direction. During normal operation, the viewing direction is changed in a repeating pattern of 16 steps to obtain full angular coverage in the elevation direction (Fig. 8). The angular pixel sizes obtained in azimuth and elevation are between $12° \times 6.3°$ and $16° \times 17°$ (Table 3).

Table 1 Requirement matrix

Property	Measurement requirement	Justification	NILS performance
Particles	Negative ions, electrons	Solar wind-surface interaction products	Negative ions, electrons
Energy range	30 eV - 1000 eV, Ions and electrons	Solar wind proton energy defined the upper limit, sputtered particles define the lower limit	3 eV - 2820 eV, Ions and electrons
Mass resolution	e^-, H^-, heavy negative ions	Hydrogen and heavier abundant species should be separated	e^- and ion mass groups centred at 1, 4, 16 and 28 amu/q
Energy resolution	<15%	Solar wind temperature	14%
Angular resolution		Separate precipitating and surface emitted particle populations	120° wide vertically oriented field of view with 16 angular pixels
Time resolution	1 min	Temporal variations of solar wind	4.06 s (one direction) for both ion and electron energy spectra acquisition
Geometric factor	$> 10^{-5}$ cm^2 sr eV/eV	Detect 1% of solar wind reflected as negative hydrogen	$2.3 \cdot 10^{-4}$ cm^2 sr eV/eV centre pixel, without efficiency, energy-based definition
Mass	<1100 g		919 g without MLI
Power	< 3.4 W		2.7 W
Size			99 mm × 167 mm × 240 mm

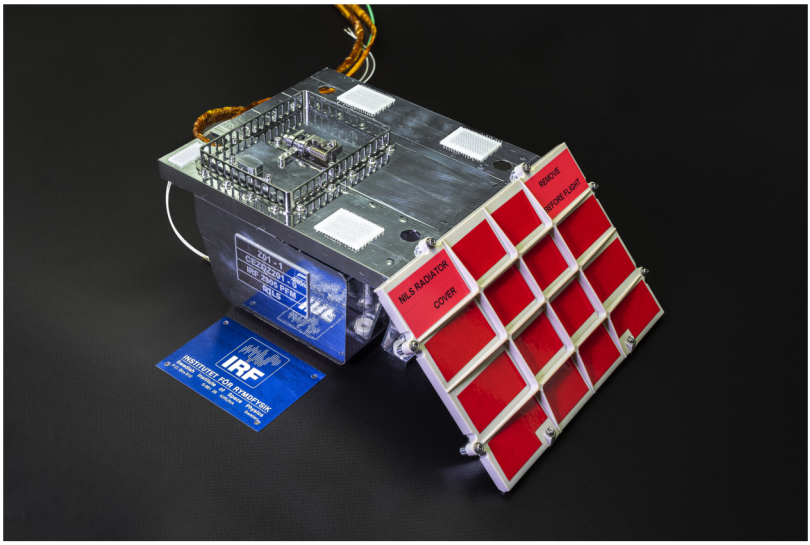

Fig. 4 Flight model of NILS. The sensor head is visible on the left with the type label mounted. The fence-like structure surrounding the entrance system keeps multi-layer insulation from protruding into the field of view. The large radiator covered by a red-tag item in the foreground ensures acceptable internal temperatures even when NILS is directly illuminated by the Sun. The white rectangular patches are multi-layer insulation (MLI) attachment points. Image: Umberto Rollero/IRF

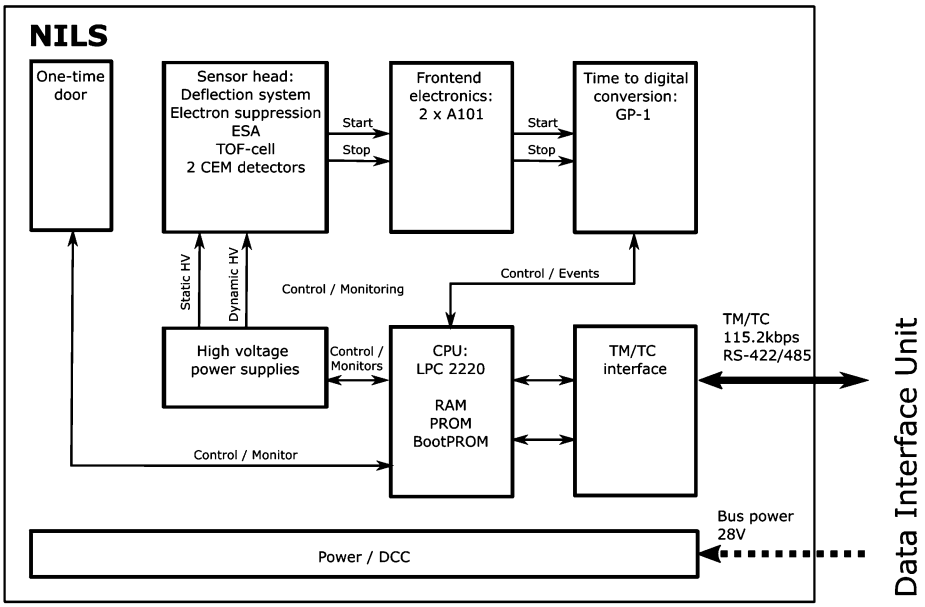

Fig. 5 NILS functional block diagram

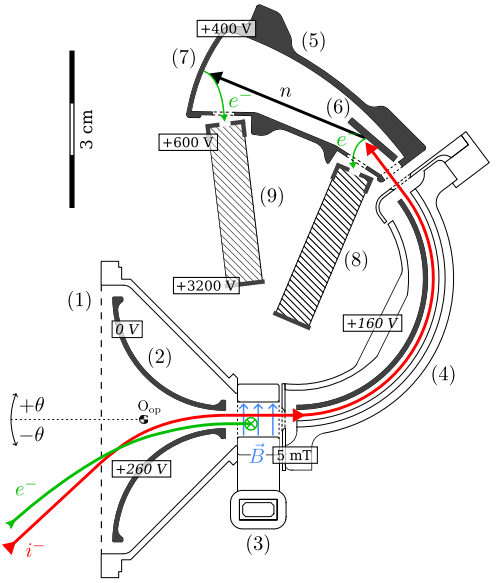

Fig. 6 Sensor head cross-section (to scale). (1) entrance grid, (2) angular deflector electrodes, (3) electron suppression system, (4) electrostatic energy analyser, (5) time-of-flight cell, (6) start surface, (7) stop surface, (8) and (9) start and stop channel electron multipliers, respectively. All high voltage electrodes are filled in black for clarity. Italicised labels indicate variable potentials, whereas normal text is used for fixed potentials. Typical particle trajectories for ions (red) and electrons (green) along with the applied electrical potentials and magnetic fields are shown for a configuration measuring negative ions with an energy of about 540 eV/q. θ indicates the elevation scanning direction, and O_{op} indicates the origin of the NILS instrument coordinate system

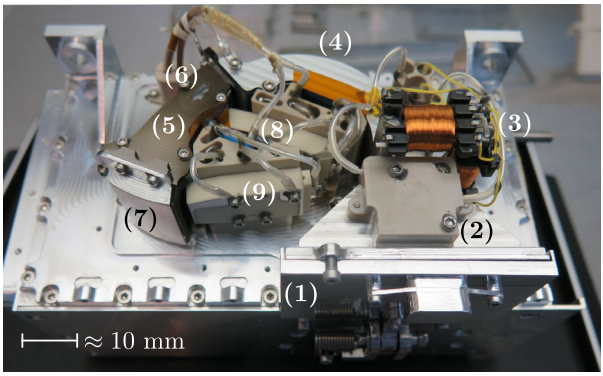

Fig. 7 NILS flight model sensor head (without cover) with the sensor door in closed configuration. The numbers are identical to those used in Fig. 6: (1) door closed hiding the sensor grid, (2) angular deflectors hidden under cover, (3) electron suppression magnet coils, hiding the iron yoke, (4) electrostatic energy analyser hidden under cover, (5) time-of-flight cell, (6) start surface hidden under cover, (7) stop surface, (8) and (9) start and stop channel electron multipliers both embedded in insulating polyether ether ketone (PEEK) blocks

2.2.2 Electron Suppression

Electrons are expected to be far more abundant than negative ions, at least at low energies. To avoid that the electron flux is saturating the time-of-flight system, a magnetic field of about 5 mT oriented perpendicular to the nominal negative ion trajectories is used to deflect electrons when measuring negative ions. The field is generated by a current through an electromagnet (Canu-Blot 2024, see Sect. 3.5). Before measuring electrons, the current through the electromagnet is reduced in an oscillating manner with an exponentially reducing amplitude until the magnetic field is close to zero.

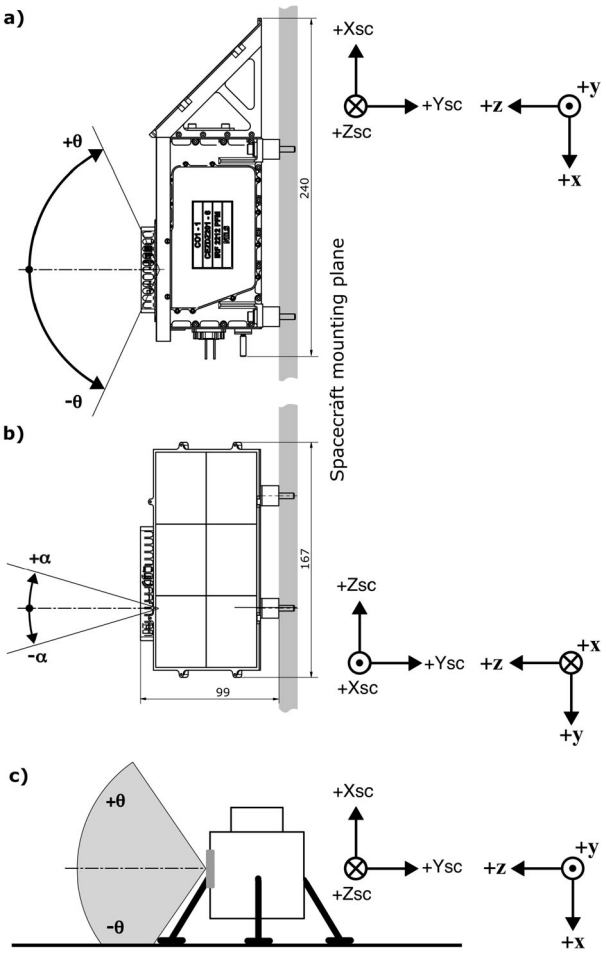

Fig. 8 Coordinate systems. X_{sc}, Y_{sc} and Z_{sc} correspond to the lander coordinate system; x, y and z to the instrument coordinate system. α and θ refer to the NILS field of view. The boresight of the field of view is aligned with the $-Y_{sc}$ direction. a) Side view, b) top view, c) accommodation on lander

When measuring negative ions, lower energy electrons up to a cutoff energy are significantly suppressed. Despite the absence of dedicated magnetic shielding, the magnetic stray field produced by the electromagnet decays to less than 10 nT at a distance of 1 m from the instrument.

2.2.3 Energy Analysis

The energy analysis is performed using a 127° electrostatic analyser with a 23 mm central radius. Compared to the cylindrical version used in the SWIM instrument (Wieser and Barabash 2016), the outer electrode of NILS has a toroidal shape to improve angular acceptance normal to the deflection plane of the electrostatic analyser. Only the inner electrode is on a positive voltage, the outer electrode is kept on ground potential to simplify the mechanical design. The inner electrode potential is swept in a monotonically increasing series of 48 different voltages, or energy steps. The energy resolution $\Delta E/E$ is approximately 0.14 for both negative ions and electrons.

2.2.4 Time-of-Flight System

A miniature surface interaction-based time-of-flight cell is used to measure the velocity of particles and ultimately determine their mass. The particles leaving the electrostatic analyser are accelerated by a potential difference of 400 V and then enter the 30 mm long time-of-flight cell. The time-of-flight start signal is generated by scattering the particles at grazing incidence on a 9 mm $\times$ 25 mm polished tungsten W(110) single crystal. A possible secondary electron produced in this process is accelerated towards a KBL408 ceramic channel electron multiplier (Sjuts Optotechnik GmbH, Göttingen, Germany) and detected as the start signal. The 400 V pre-acceleration ensures a sufficiently large secondary electron yield on the start surface. The original particle most likely looses its charge during the interaction with the start surface and is forward scattered as a neutral particle toward the Al_2O_3 coated stop surface. There again with a certain probability a secondary electron is created that is recorded by the time-of-flight stop channel electron multiplier of the same type as the start detector. Figure 6 shows typical particle trajectories.

The mass resolution is mainly limited by the statistical energy loss particles experience on the start surface and the unknown exact hit position of the particle on the start surface. The later results in an uncertainty of the actual flight path length in the time-of-flight cell. Between 6 ns and 40 ns of the measured time-of-flight peak width is attributed to these two effects. The spread of the particle velocity in the time-of-flight cell due to the finite energy resolution of the electrostatic analyser, secondary electron travel times to the detectors, variations in the propagation delays of the electron clouds in the channel electron multipliers and a pulse height dependent propagation delay in the pre-amplifiers contribute additional 9 ns. All effects combined, this results in a final mass resolution of the system of $m/\Delta m \approx 2$.

2.2.5 Ultraviolet Suppression

The Sun may be in the field of view of NILS making sufficient suppression of ultraviolet photons necessary. Internal ion optical surfaces are coated with Acktar Magic black (Acktar Ltd., Kiryat-Gat, Israel). This coating has a hemispherical reflectance of about 2% in the ultraviolet range. Combined with that only a small solid angle after each reflection is pointing in a suitable direction for the photons to penetrate deeper into the instrument, each reflection in the instrument reduces the ultraviolet photon flux about by a factor of 10^3. Combined with the suppression originating from the time-of-flight system, an estimated total ultraviolet photon suppression of $> 10^8$ is achieved.

2.2.6 Electronics

NILS uses the same electronics architecture as the ASAN instrument (Wieser et al. 2020). Three stacked electronics boards accommodate the high voltage power supplies, the front-end electronics and the digital processing unit, and the low voltage power system.

The high voltage board provides the main high voltages of $+4$ kV and -4 kV respectively. All other high voltages are regulated from the main high voltages using in-house-built high voltage opto-couplers. There are three fast changing high voltages that are connected to the electrostatic analyser and the elevation system electrodes and a number of static high voltages, for example used to bias the channel electron multipliers. The high voltage board also contains all the analog-to-digital (ADC) and digital-to-analog (DAC) converters needed for control of the high voltage levels and for housekeeping. Additionally, the high voltage board also accommodates the regulated current supply for the electron suppression magnet.

The front-end and digital processing board contains pre-amplifiers, the time-to-digital converter, the instruments' microprocessor with an associated 64 kByte PROM for the software, and the telemetry interface. Two Amptek A101 pre-amplifiers convert the current pulses provided by the time-of-flight start and stop detectors to digital signals. A TDC-GP1 Time-to-Digital Converter (acam-messelectronic GmbH, Stutensee-Blankenloch, Germany) is used to measure the time-of-flight by measuring the time difference between start and stop signals. The data acquisition and processing and the telemetry and command interface are controlled by a LPC2220 ARM microcontroller. A 4 kByte serial EEPROM contains additional instrument configuration that can be updated using tele-commands. The command and telemetry interface is a 112.5 kbps bidirectional RS422/485 link.

The low voltage power board interfaces the 28 V spacecraft power bus. An inrush current limiter eliminates large peak currents during instrument startup. A galvanically insulated direct current converter provides all NILS internal voltages: +3.3 V, +5 V, +12 V and −12 V. The low voltage power board also contains the driver circuit for the wire-burn resistors releasing the spring-loaded hatch protecting the entrance system from dust during the landing on the Moon.

2.2.7 Thermal Design

The instrument is mounted on the sunlit side of the lander (see Fig. 8), exposing it to significant direct solar illumination as well as to radiation from the illuminated lunar surface. Given the landing local time and location, the expected thermal power transferred to the instrument due to solar illumination is about 5 W. Infrared radiation from the surface results in additional 0.5 W influx to the instrument.

To minimize the thermal impact on the lander, the instrument was required to be thermally decoupled from the lander. Conductive heat transfer was minimized by mounting the instrument using 12.4 mm thick epoxy isolators and titanium screws, which have low thermal conductivity. Radiative heat exchange between the instrument and the lander is minimized by the use of surface treatments, resulting in a low emissivity on the lander-facing side of the instrument. Polished aluminium or vapour-deposited aluminium tape is used. The total heat transfer from the instrument the lander is therefore only 0.4 W. The instrument has an internal power dissipation of 2.7 W, equally distributed across its three main electronics boards.

To minimize the radiative heat input from the environment, the instrument is almost entirely covered with multi-layer insulation (MLI). Only the radiator and the entrance aperture are exposed. The heat influx through the entrance aperture is the main contribution to the heat influx.

A 150 mm × 100 mm large radiator covered with optical solar reflectors (OSR) allows keeping the nominal instrument temperature for a sufficiently long time below 70 °C to reach mission success. The radiator is inclined 45° from the vertical mounting panel to lower the viewing factor of the lunar surface and to increase the viewing factor of the sky. The dimensioning of the radiator takes into account the possible degradation resulting from lunar dust deposition during landing.

During cruise, the spacecraft attitude results in the instrument being mostly in the shadow. The effective cooling provided by the thermal radiator makes a survival heater necessary. The installed heater has a power dissipation of 8 W and is connected in series to a thermally activated switch that closes when the temperature is below −20 °C. The switching temperature is fixed and can not be changed without exchanging the hardware.

2.2.8 Protective Cover

The aperture of the instrument is protected by a spring-loaded cover. The selected mechanism is identical to the one used in the ASAN instrument (Wieser et al. 2020). The cover reduces the risk of particle contamination of the entrance system during landing on the Moon. After landing, the door is opened as a first step in the NILS operation sequence (Sect. 11). Before landing, the cover is kept in closed position by a UHMwPE (Ultra High Molecular weight Polyethylene) string routed across two redundant high temperature resistors. To open the cover, the resistors are energized for a maximum duration of 30 s. In the process, the resistors reach temperatures up to 200 °C. This will melt the string, and thus release the cover. The cover state is determined by a micro-switch that closes when the cover is fully open. As the cover is spring-loaded, once the cover is opened, it cannot be closed again.

3 Calibration Setup

The NILS instrument underwent calibration at the Swedish Institute of Space Physics in Kiruna, Sweden. The calibration facility is equipped to produce positively charged ion beams that span energies from 30 eV/q to 50 keV/q. The mass separation of the beam is achieved using a Wien filter placed in the beam line. Monitoring of beam intensity is ensured through a high-transparency grid, complemented by a removable Faraday cup for total intensity measurements. The beam intensity typically ranged from 0.1 to 10 nA. The instrument itself is mounted on a four-axis turntable, enabling both translation and rotation movements with respect to the calibration beam. The turntable operates autonomously, executing complex predefined scanning patterns without requiring user intervention. The entire setup is housed within a vacuum chamber of 1200 mm diameter, maintaining a base pressure in the main chamber of approximately 10^{-7} mbar. Figure 9 shows the calibration setup with all the aforementioned components (Canu-Blot 2024, see Sect. 4.1).

The NILS instrument was calibrated using electrons, H^-, and O^- ions. Since the calibration facility does not natively produce negatively charged ions, a surface-interaction-based positive-to-negative charge state converter, referred to as the Negative IOn Source (NIOS, Fig. 10), was developed (Wecker 2024). In the NIOS, a primary positive ion beam strikes a highly polished aluminium conversion surface at grazing angles. A small fraction charge exchanges on the surface to negative ions. A set of electrodes, set to a negative potential V_{NIOS} relative to the conversion surface, electrostatically guide the negative ions towards the exit aperture. These negative ions have a broad energy distribution, with a maximum energy close to the impinging positive ion energy. The remaining positive and neutral particles are deflected and absorbed. In the case of molecular primary ions, most molecules dissociate on the conversion surface resulting in atomic negative ions with a maximum kinetic energy close to the kinetic energy the individual atoms had when it was part of the molecule.[1] Additionally, some secondary electrons from the field-shaping electrodes exit the NIOS at an energy close to the electrode potential. The combined population of negative ions and electrons serves as a calibration source for the NILS instrument.

[1] A typical use case is primary H_2^+ converting to H^-.

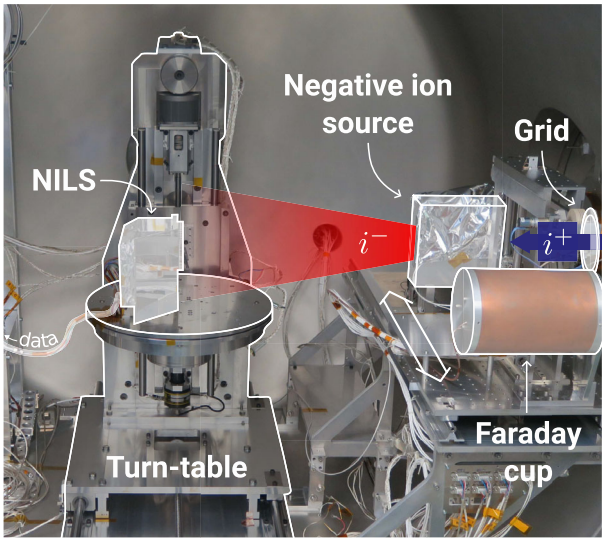

Fig. 9 The NILS flight model inside the calibration chamber, with all major calibration units labelled. A positive ion beam (blue) is injected from the right through a 90% transparency grid into the negative ion source, generating a divergent negative ion beam (red). The grid continuously measures the beam's relative density, while a movable Faraday cup provides absolute density measurements. Both the Faraday cup and the negative ion source are mounted on a translatable table. The NILS instrument is positioned on a 4-axis turntable, enabling both rotational and translational movements. Data from the instrument are transmitted through a vacuum chamber feed-through to the calibration computer system

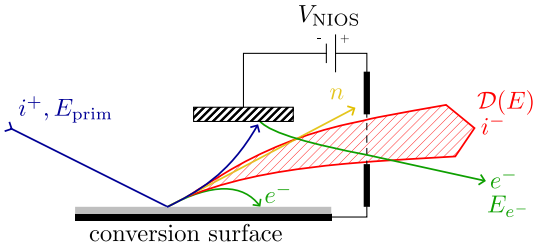

Fig. 10 The Negative Ion Source (NIOS) principles of operation. Positive ions i^+ are shown in blue, energetic neutral atoms n in yellow, negative ions i^- in red and secondary electrons e^- in green. The energy distributions for positive ions, negative ions and electrons exciting the NIOS are noted E_{prim}, $\mathcal{D}$ and E_{e^-}, respectively. V_{NIOS} is the voltage applied to the NIOS internal field-shaping electrodes. Secondary electrons are also generated at the conversion surface, but their low energy prevents them from leaving NIOS

4 Performance

4.1 Theory of Measurement

In this section, we establish the terminology used throughout subsequent sections, outlining the framework for describing the response of the instrument to the typical ion- and electron-populations measured by the NILS instrument.

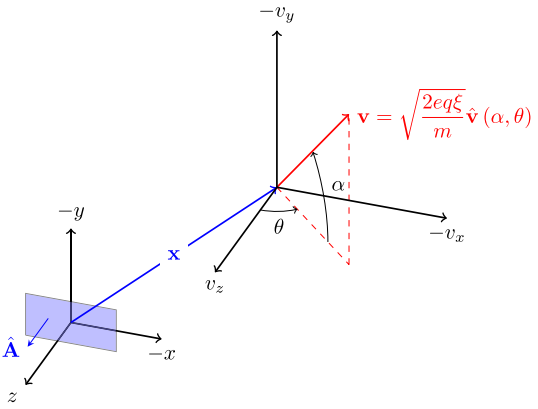

Fig. 11 Definition of the physical and velocity spaces. The light blue rectangle shows the orientation of the instrument effective area (the coordinates x, y, z are similar to those in Fig. 8). At each position $\mathbf{x}$ in the physical space, a particle velocity is defined by a position vector $\mathbf{v}$ in velocity space

4.1.1 Phase Space and Phase Space Density

We consider a particle i of species γ, defined by its charge q and mass m. At a time t, the position of the particle $\mathbf{x}_i(t)$ is a point in a 3-dimensional physical space. It is useful to define the velocity of the particle $\mathbf{v}_i(t) = \mathrm{d}\mathbf{x}_i(t)/\mathrm{d}t$ as a point in a 3-dimensional velocity space. Together, the 3-dimensional physical and velocity spaces form a 6-dimensional phase space (see Fig. 11), with coordinates $(\mathbf{x}, \mathbf{v}) = (x, y, z, v_x, v_y, v_z)$. At any given time, the dynamic state of a N-particle system is fully described by N points in the phase space, with the exact phase space density of a particle i defined through 3-dimensional Delta Dirac functions as follows:

$$f_i(t) = \delta(\mathbf{x} - \mathbf{x}_i(t)) \cdot \delta(\mathbf{v} - \mathbf{v}_i(t)) \left[\mathrm{s}^3/\mathrm{m}^6\right]. \tag{1}$$

Rather than focusing on individual particles, it is more practical to describe a system statistically, that is for a large enough number of identical particles. For this statistical approach, consider a tiny 3-dimensional volume $d\mathbf{x}$ centred on the location $\mathbf{x}$ in physical space, and similarly the tiny 3-dimensional volume $d\mathbf{v}$ centred on the location $\mathbf{v}$ in velocity space,[2] both defined as follows:

$$\begin{aligned} \mathrm{d}\mathbf{x}(x, y, z) &= \mathrm{d}x \cdot \mathrm{d}y \cdot \mathrm{d}z \left[\mathrm{m}^3\right], \\ \mathrm{d}\mathbf{v}(v_x, v_y, v_z) &= \mathrm{d}v_x \cdot \mathrm{d}v_y \cdot \mathrm{d}v_z \left[\mathrm{m}^3/\mathrm{s}^3\right]. \end{aligned} \tag{2}$$

The phase space density $f_\gamma(\mathbf{x}, \mathbf{v}, t)$ $\left[s^3/m^6\right]$ of the particle system therefore defines the number of particles N of species γ at an instant t contained within the small phase space volume element $\mathrm{d}\mathbf{x}\mathrm{d}\mathbf{v}$ centred about the phase space position $(\mathbf{x}, \mathbf{v})$:

$$f_\gamma(\mathbf{x}, \mathbf{v}, t) \equiv \frac{N(t)}{\mathrm{d}\mathbf{x}\mathrm{d}\mathbf{v}} \left[\mathrm{s}^3/\mathrm{m}^6\right]. \tag{3}$$

4.1.2 Instrument Response Function

In the most general sense, the instrument conducts a measurement of the particle phase space density over a confined region of the phase space. For different voltage configurations of the

[2] Both volumes should be regarded as finite, rather than infinitesimally small. They must be sufficiently small relative to the system spatial and velocity variation scales, yet large enough to contain enough particles for statistical description.

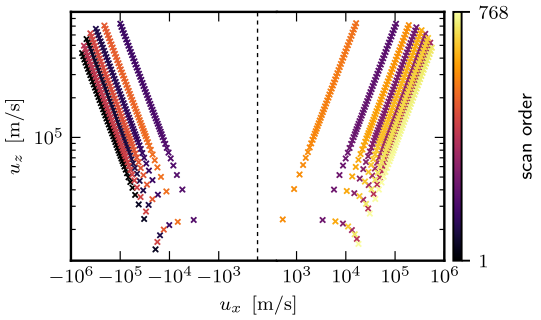

Fig. 12 Scanning coverage of the **u**-space for negative hydrogen ions. Each cross represents a measurement setting, each row of crosses represents a single energy scan. The color shows the measurement order (see Fig. 31) of the 16 elevation steps × 48 energy steps = 768 different measurement settings

instrument electrodes, the instrument observes different regions of the phase space. These regions are not observed uniformly, as the instrument sensitivity varies with the particle energy, direction, mass, charge, with time, and other factors.

For a given voltage configuration (see Fig. 6 for an example of a specific voltage configuration of the instrument electrodes), the response of the instrument to an external flux of particles is characterised by its (unit-less) response function $\mathcal{R}_\gamma(\mathbf{x}, \mathbf{v}, t)$. This function gives the probability of detecting a particle of species γ with position $\mathbf{x}$ and velocity $\mathbf{v}$ in the phase space at time t. We additionally define the ideal instrument response $\mathcal{R}_0$ as a Boolean function: either the particle is detected or not:

$$\mathcal{R}_0(\mathbf{x}, \mathbf{v}, t) \equiv \begin{cases} 1 & \text{if } \mathcal{R}_\gamma(\mathbf{x}, \mathbf{v}, t) > 0 \\ 0 & \text{otherwise} \end{cases}. \tag{4}$$

Measurement Setting The NILS instrument performs measurements using 16 different elevation steps and 48 energy steps (see Sects. 2.2.1 and 2.2.3), each associated with a unique electrode voltage configuration. To simplify subsequent analysis, we label each pair of elevation and energy steps by a velocity vector **u** (Vasyliunas 1971, p. 75), thereafter called the "measurement setting". For a given particle species γ and time t, the measurement setting **u** is defined as the average velocity of the detected particles:

$$\mathbf{u} \equiv \frac{\langle \mathbf{v}\mathcal{R} \rangle}{\langle \mathcal{R} \rangle}, \tag{5}$$

with $\langle \cdot \rangle$ the arithmetic mean over the support of the function. The direction and magnitude of **u** therefore provide an average representation of a measurement in the velocity space. The instrument response function corresponding to each measurement setting **u** is written as $\mathcal{R}_\gamma(\mathbf{u}, \mathbf{x}, \mathbf{v}, t)$.

During a complete measurement cycle, the NILS instrument samples the velocity space from a discrete set of measurement settings corresponding to a series of points in **u**-space. This **u**-space is aligned with the velocity space depicted in Fig. 11. Figure 12 illustrates the scanning scheme in **u**-space for negative hydrogen ions with 48 energy steps and 16 direction (or elevation) steps as employed by NILS.

Instrument Coordinates In practice, the instrument scans the velocity space using a discrete set of directions $\hat{\mathbf{v}}$, particle absolute energy-per-charge ratios ξ $\left[\mathrm{eV/q}\right]$, and particle masses m $\left[\mathrm{kg}\right]$. Expressing the unit vector $\hat{\mathbf{v}}$ as a function of the instrument spherical angles (α, θ)

illustrated in Fig. 11, we obtain the relation

$$\frac{m\,\mathbf{v}^2}{2} = e\,q\,\xi\,\hat{\mathbf{v}}\,(\alpha,\theta)\,, \tag{6}$$

with e [C] the elementary charge and $q \in \mathbb{Z}^+$ the absolute charge state of the particle. The coordinate system used by the NILS instrument is therefore defined as the energy-spherical coordinate system (ξ, α, θ), with $\alpha \in [-\pi/2, \pi/2)$ and $\theta \in [0, 2\pi)$.

4.1.3 Observation of the Particle Phase Space Density Function

For each measurement setting $\mathbf{u}$, the instrument reports the number of counts $\mathcal{C}$ observed during the measurement integration time τ. For a particle species γ characterised by a phase space density $f_\gamma\,(\mathbf{x}, \mathbf{v}, t)$, the number of particles detected by the instrument at a given time t is expressed as:

$$\mathcal{C}_\gamma\,(\mathbf{u}, t) \equiv \iint \mathcal{R}_\gamma\,(\mathbf{u}, \mathbf{x}, \mathbf{v}, t)\,f_\gamma\,(\mathbf{x}, \mathbf{v}, t)\,d\mathbf{x}d\mathbf{v}. \tag{7}$$

In the case of NILS, the integration over the physical space is achieved by counting the number of particles intersecting an effective area $\mathbf{A}(\mathbf{u})$ over the integration time τ: $\int d\mathbf{x} = \int_\tau \int_{\mathbf{A}} \mathbf{v} \cdot d\mathbf{A}dt$. In that case, Eq. (7) becomes:

$$\mathcal{C}_\gamma\,(\mathbf{u}, t) = \int_t^{t+\tau} \int \left(\int_{\mathbf{A}(\mathbf{u})} \mathcal{R}_\gamma\,(\mathbf{u}, \mathbf{x}, \mathbf{v}, t)\,f_\gamma\,(\mathbf{x}, \mathbf{v}, t)\,\mathbf{v} \cdot d\mathbf{A} \right) d\mathbf{v}dt, \tag{8}$$

The effective area $\mathbf{A}\,(\mathbf{u}) = A\,(\mathbf{u})\,\hat{\mathbf{A}}$ is defined as the smallest area crossed by all particles detected by the instrument for a given setting $\mathbf{u}$.[3] The orientation of this surface is chosen along the outward normal $\hat{\mathbf{A}}$ of the instrument aperture (Fig. 11). Assuming the phase-space density and the instrument response are constant over the effective area and integration time interval, Eq. (8) can be rewritten as:

$$\frac{\mathcal{C}_\gamma\,(\mathbf{u})}{\tau} = \mathbf{A}\,(\mathbf{u}) \cdot \int \mathbf{v}\mathcal{R}_\gamma\,(\mathbf{u}, \mathbf{v})\,f_\gamma\,(\mathbf{v})\,d\mathbf{v}, \tag{9}$$

To simplify the notation, we consider a single particle species and thereafter drop the subscript γ. Equation (9) addresses the fundamental challenge of any particle instrument, that is, what can we say about that underlying phase-space density function $f\,(\mathbf{v})$ given a discrete set of observations $\mathcal{C}\,(\mathbf{u})$?

4.2 Independent Angular and Energy Responses

Instruments employing an electrostatic angular deflector followed by an electrostatic energy analyser often exhibit coupling between both two systems. In other words, depending on the viewing direction selected by the angular deflector, the response of the energy analyser varies.

[3] Often $A\,(\mathbf{u})$ is reasonably well approximated by the geometric entrance aperture of the instrument and thus independent of $\mathbf{u}$, but this is strictly only true for the most simple instrument geometry where the entrance aperture is the only element that constrains $A\,(\mathbf{u})$ in any way.

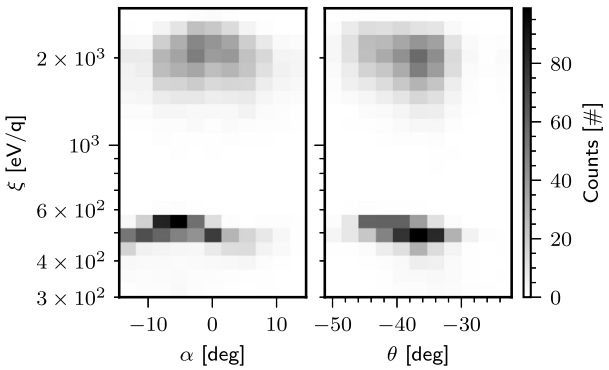

Fig. 13 Energy-angular response of the start detector to a flux of H^- ions and electrons. The observed energy distributions of both negative ions and electrons demonstrate that there is only a weak dependence on the viewing angles, supporting our simplifying assumption of independence between the energy and angular responses

The angular deflector and energy analyser in the NILS sensor are spatially separated by the electron suppression magnet. This separation leads to a weaker ion-optical coupling between the deflector and the analyser. This weak dependence is illustrated in Fig. 13, where the observed energy distributions of two negatively charged particle populations only weakly depend on the instrument viewing angles. From now on, we neglect any dependence, allowing us to write

$$\mathcal{R}\left(\mathbf{u}, \xi, \theta, \alpha\right) \approx \kappa\left(\mathbf{u}\right) \mathcal{R}_{\Omega}\left(\mathbf{u}, \theta, \alpha\right) \mathcal{R}_{E}\left(\mathbf{u}, \xi\right), \tag{10}$$

where $\mathcal{R}\left[\cdot\right]$ is the unit-less probability function defining the instrument response, $\mathcal{R}_{\Omega}\left[\mathrm{sr}^{-1}\right]$ and $\mathcal{R}_{E}\left[\mathrm{q/eV}\right]$ are normalised functions (whose integral over the definition domain is equal to one) defining the shape of the instrument angular and energy responses, respectively. Finally, $\kappa\left[\mathrm{sr} \cdot \mathrm{eV/q}\right]$ is a scaling factor that accounts for the real amplitude of the response functions.

4.3 Energy Response

As introduced in Sect. 2.2.3, the instrument uses an electrostatic energy analyser that employs electrostatic fields to allow the passage of charged particles with a specified energy-to-charge ratio ξ. For a measurement setting $\mathbf{u}$, the energy response of the analyser is well approximated by a Normal distribution $\mathcal{N}$ centred at ξ_u with a full-width at half-maximum of $\Delta\xi_u$ (see Fig. 14):

$$\begin{aligned} \mathcal{R}_{E}\left(\mathbf{u}, \xi\right) &\equiv \mathcal{N}\left(\xi; \xi_u, \Delta\xi_u\right), \\ \Delta\xi_u &\equiv \xi_u E_{\mathrm{res}}, \end{aligned} \tag{11}$$

where ξ_u and $\Delta\xi_u$ refer to the average energy-per-charge and energy-per-charge width of the measurement $\mathbf{u}$, as derived from Eq. (5), and E_{res} is the energy resolution (see Sect. 4.3.3).

4.3.1 Calibration with Electrons

Estimating the instrument energy response requires accurate knowledge of the calibration beam energy distribution. Ideally, particle instruments are calibrated over a homogeneous and mono-energetic beam of known energy. However, in our application, the negative ion calibration beam is obtained from charge-exchange at a conversion surface, which, with the addition of electrostatic filtering of the resulting charge states, leads to a broad energy

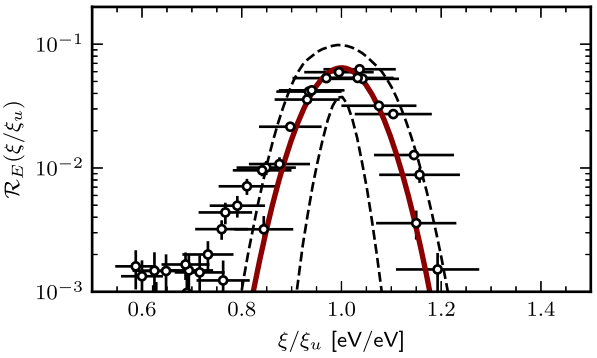

Fig. 14 Energy response function normalised to the energy bin centre ξ_u. Calibration data (open circles) are shown together with the energy response function as defined in Eq. (11). The dotted lines represent a 90% confidence limit on the response function estimate

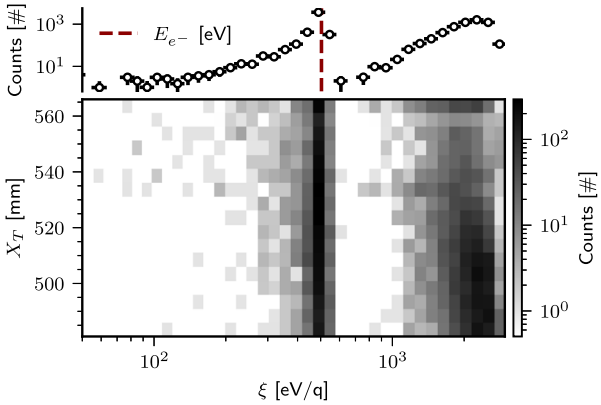

Fig. 15 The energy-position response of the instrument under the NIOS for a primary beam energy of 5 keV H_2^+. X_T represents to the translation of NILS entrance aperture relative to the NIOS source exit (Fig. 24) and ξ is the energy setting of the electrostatic analyser. Two clear populations are observed: the negative dissociated hydrogen ions at around 2.4 keV and the electrons at 500 eV. The negative ions display a broader energy distribution, whereas the electron distribution is narrow, peaking about at the potential of the NIOS electrodes shown by the vertical dashed line

distribution (Fig. 15). Instead, another negatively charged population was used to characterise the instrument energy response: the secondary electrons originating from the NIOS internal electrodes. These electrodes are maintained at a fixed negative voltage V_{NIOS} [V] (see Sect. 5.3.1). Secondary electrons are generated when atoms and ions that scatter within the NIOS collide with these electrodes. Secondary electrons typically have an energy of $E_{\mathrm{S}} \approx 2$ eV upon emission and are subsequently accelerated toward the chamber ground potential, reaching a maximum energy of $E_{e^-} \approx -eV_{\mathrm{NIOS}}/\mathrm{eV} + E_{\mathrm{S}}$, with eV the electronvolt constant. We call such electrons exiting the NIOS and detected by NILS "NIOS electrons".

Since no other force is likely to accelerate these electrons, we can assume that their energy distribution is limited by E_{e^-}. Figure 15 illustrates an example of the energy distribution of electrons exiting the NIOS. Given that the low-energy tail minimally contributes to the total electron flux, we initially assume that the NIOS electrons exhibit a nearly monoenergetic distribution. It is from this population that we calibrate the energy response function of the NILS instrument.

4.3.2 Electrostatic Analyser Constant

The electrostatic nature of the system allows for a directly proportional relationship between the voltage V_{ESA} present between the two electrostatic analyser electrodes and the average energy-to-charge ratio ξ_u of the particles accepted by the system. Throughout this paper, we define ξ as a positive number despite measuring negative charges. Thus, we define the positive dimensionless analyser constant $\mathcal{K}$ as[4]

$$\xi_u = \mathcal{K}\,|V_{\mathrm{ESA}}|\ . \tag{12}$$

The analyser constant is estimated from NIOS electrons as shown in Fig. 15. Their energy is finely constrained by the NIOS internal electrode voltage. The constant $\mathcal{K}$ typically varies with the elevation angle θ due to the asymmetry of the electrostatic analyser. However, this variation is small for the NILS instrument; the analyser constant varies less than 5% within the full elevation range of the instrument. Including this effect, we obtain the best estimate of the analyser constant of $\hat{\mathcal{K}} \approx 3.59 \pm 0.1\ (1\sigma)$.

4.3.3 Energy Resolution

The electrostatic analyser accepts charged particles within an energy pass band whose shape is solely determined by the geometry of the analyser. The energy response can be approximated as a Normal distribution, with the width $\Delta\xi_u$ corresponding to its full-width at half-maximum (Fig. 14). Due to the electrostatic nature of the analyser, the ratio $E_{\mathrm{res}} = \Delta\xi_u/\xi_u$ remains constant for all ξ_u.

Observations show that the energy distribution of NIOS electrons is narrower than that of negative ions, although not following a Dirac-like distribution. There is an observable energy broadening, likely attributed to energy-angular sorting of the electrons as a result of the magnetic field of the Earth. To account for the energy spread of the NIOS electrons in the estimation of E_{res}, we empirically describe the observed energy resolution by a shifted Weibull distribution

$$f\left(E_{\mathrm{res}};\lambda,k,c\right) = \begin{cases} \dfrac{k}{\lambda}\left(\dfrac{E_{\mathrm{res}}-c}{\lambda}\right)^{k-1} & \\ \cdot\ \exp\left(\dfrac{c-E_{\mathrm{res}}}{\lambda}\right)^{k} & \text{if } E_{\mathrm{res}} \geq c \\ 0 & \text{if } E_{\mathrm{res}} < 0 \end{cases}, \tag{13}$$

with λ and c the parameters of the distribution and $k \in (0, 2)$ such that

$$\left.\frac{\partial f}{\partial E_{\mathrm{res}}}\right|_{E_{\mathrm{res}}=c} \to \infty. \tag{14}$$

The parameter c is the best estimate of the energy resolution. By using a non-linear least-square to fit the distribution to the data binned following the Freedman–Diaconis rule (Freedman and Diaconis 1981), we can estimate the cutoff parameter c along with its uncertainty. The resulting best estimate of the energy resolution is $\hat{E}_{\mathrm{res}} = 14\%$, with a 90% confidence interval of $[8, 14]\,\%$.

[4] An exhaustive definition of $\mathcal{K}$ in the context of the NILS instrument can be found in Canu-Blot (2024, Sect. 3.3.2).

Table 2 Energy bin (or step) number to the average energy-to-charge ratio ξ_u lookup table. The relative error on ξ_u is estimated to be ranging from 3% at high energies up to 20% at the lowest four energies. Estimates are given with three significant digits, except for the lowest four energies

Energy bin number	ξ_u [eV/q]	Energy bin number	ξ_u [eV/q]
0	2820	24	209
1	2520	25	189
2	2260	26	170
3	2020	27	154
4	1810	28	139
5	1620	29	126
6	1460	30	114
7	1300	31	103
8	1170	32	93.6
9	1050	33	85.1
10	940	34	77.4
11	842	35	70.6
12	755	36	64.5
13	678	37	59.0
14	608	38	53.4
15	545	39	47.8
16	490	40	42.2
17	440	41	36.6
18	395	42	31.0
19	355	43	25.4
20	319	44	20.
21	287	45	14.
22	258	46	9.
23	232	47	3.

4.4 Angular Response

The NILS instrument features a fan-shaped field of view (Fig. 8), mechanically constrained by the obstruction from the fence-like mechanical structure that prevents the multi-layer insulation from blocking the field of view. The unobstructed field of view covers $\pm 60°$, centred around the elevation angle $\theta = 0°$. This field of view is divided into 16 different angular viewing directions, incrementally scanned by the single angular pixel of the instrument.

The simple construction of the elevation scanning system results in a different shape of the angular response function versus the elevation angle. For one specific viewing direction, the instrument angular response function can be well-approximated by a modified bivariate Normal distribution (Fig. 16), defined as

$$\mathcal{R}_\Omega(\mathbf{u},\theta,\alpha) \equiv \frac{\kappa_\Omega(\mathbf{u})}{2\pi\sigma_\theta(\mathbf{u})\sigma_\alpha(\mathbf{u})} \exp\left[\frac{(\alpha-\alpha_u)^2}{2\sigma_\alpha(\mathbf{u})^2} - \frac{(\theta-\theta_0(\mathbf{u},\alpha))^2}{2\sigma_\theta(\mathbf{u})^2}\right] \tag{15}$$
$$\theta_0(\mathbf{u},\alpha) = \theta_u + s(\mathbf{u})\cdot(\alpha-\alpha_u)^2 ,$$

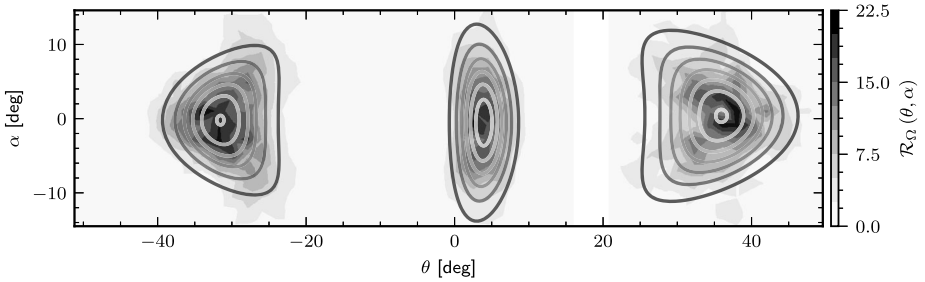

Fig. 16 Examples of the angular response $\mathcal{R}_\Omega(\mathbf{u}, \theta, \alpha)$ as measured during the calibration campaign for a central-looking and two side-looking angular pixels. The fit function given in the Eq. (15) is fitted to all three responses. The actual viewing directions selected for the flight unit are shown in Fig. 17

Table 3 Angular bin to angular response parameters: the average elevation angle θ_u, solid angle $\Delta\Omega$ at half of the response peak, and the maximum angular spread in α and θ at half of the response peak for each elevation bin D. The uncertainty in the response's solid angle is given in terms of one standard deviation. The uncertainty (one standard deviation) in θ_u is about one degree for all elevation steps

Angular bin D_n	θ_u [deg]	$\Delta\Omega \pm \sigma_{\Delta\Omega}$, 10^{-2} [sr]	$\Delta\alpha$ [deg]	$\Delta\theta$ [deg]
0	52	4.7 ± 0.62	12	17
1	39	4.0 ± 0.28	13	13
2	24	3.1 ± 0.23	15	8.7
3	7.4	2.5 ± 0.24	16	6.5
4	−7.5	2.4 ± 0.26	16	6.3
5	−20	2.7 ± 0.24	15	7.5
6	−32	3.2 ± 0.34	14	9.7
7	−43	3.8 ± 0.65	13	12
8	46	4.4 ± 0.39	12	15
9	32	3.6 ± 0.19	14	11
10	16	2.7 ± 0.26	15	7.4
11	−1.0	2.3 ± 0.25	16	6.2
12	−14	2.5 ± 0.23	15	6.8
13	−26	2.9 ± 0.28	14	8.5
14	−38	3.5 ± 0.51	13	11
15	−48	4.0 ± 0.82	12	14

with (θ, α) the viewing angles in degrees, θ_u the average elevation angle for the measurement $\mathbf{u}$ as tabulated in Table 3, and κ_Ω a normalization factor such that $\iint \mathcal{R}_\Omega \cos\alpha \mathrm{d}\alpha \mathrm{d}\theta = 1$. After fitting all available angular scans, we derived the following parameters of the angular response function:

$$\begin{aligned} \alpha_u &= -7.52 \times 10^{-1} \left[\mathrm{deg}\right] \\ s(\mathbf{u}) &= -1.61 \times 10^{-3} \cdot \theta_u - 3.02 \times 10^{-3}, \\ \sigma_\theta(\mathbf{u}) &= 1.48 \times 10^{-3} \cdot \theta_u^2 + 6.14 \times 10^{-3} \cdot \theta_u + 2.64, \\ \sigma_\alpha(\mathbf{u}) &= -6.35 \times 10^{-4} \cdot \theta_u^2 + 1.65 \times 10^{-3} \cdot \theta_u + 6.68. \end{aligned} \tag{16}$$

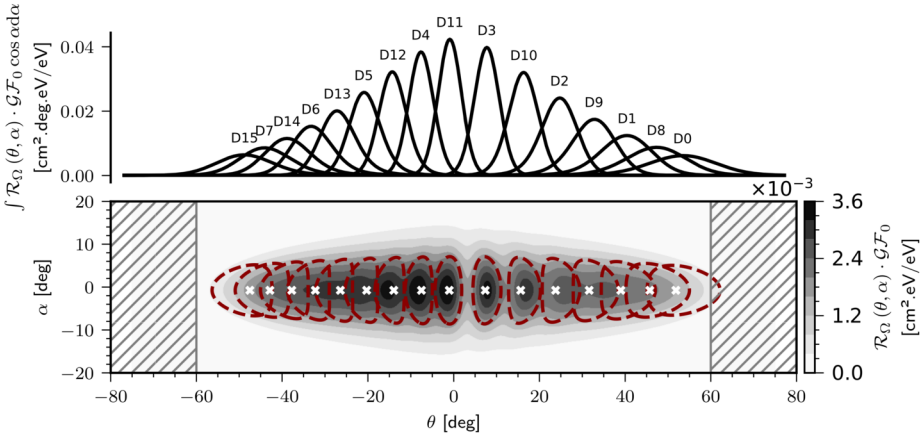

Fig. 17 Nominal phase-space coverage as a function of the viewing angles. The angular response function is weighted by the geometric factor calculated in Sect. 5. Red dashed lines indicate the half-maximum contour for each of the 16 elevation steps, while white crosses mark the average elevation and azimuthal angles at each step, ie. (θ_u, α_u). The hatched region represents areas obstructed by the multi-layer insulation surrounding the instrument

Table 3 summarizes the nominal elevation angles and key characteristics of the angular response for each of the 16 elevation steps. Figure 17 provides an overview of the total field of view of the instrument and its nominal phase-space coverage, representing its sensitivity across the field of view.

4.4.1 Elevation Scanning Constant

Similarly to the energy analyser, the deflection of charged particles within the elevation scanning system relies on an electrostatic system. Therefore, we introduce another dimensionless constant, which represents the proportionality factor between the potential difference $\Delta V_{\text{defl}} \equiv V_{\text{defl}}^{\text{up}} - V_{\text{defl}}^{\text{down}}$ [V] applied across the deflector electrodes and the average energy-to-charge ratio ξ_u of the deflected particles for a specific measurement $\mathbf{u}$:

$$\Gamma(\theta_u) \equiv \frac{\Delta V_{\text{defl}}(\theta_u)}{\xi_u}. \tag{17}$$

The factor Γ depends only on the average elevation angle θ_u of a particular measurement. The relation between Γ and the average elevation angle θ_u in degrees is empirically approximated by the linear function

$$\Gamma(\theta_u) \approx k_1\theta_u + k_2\,, \tag{18}$$

with $k_1 = 7.2 \times 10^{-3}$ and $k_2 = -2.4 \times 10^{-2}$. Equation (17) can be inverted to construct high-voltage settings for the electrodes of the elevation scanning system based on the desired viewing direction $\theta_u(D)$ for the elevation step D, giving

$$\Delta V_{\text{defl}}[\theta_u(D)] = \xi_u \cdot \Gamma[\theta_u(D)]\,. \tag{19}$$

After the flight unit was delivered, additional offset voltages in the high-voltage system driving the elevation scanning electrodes were discovered. These voltage offsets could not be

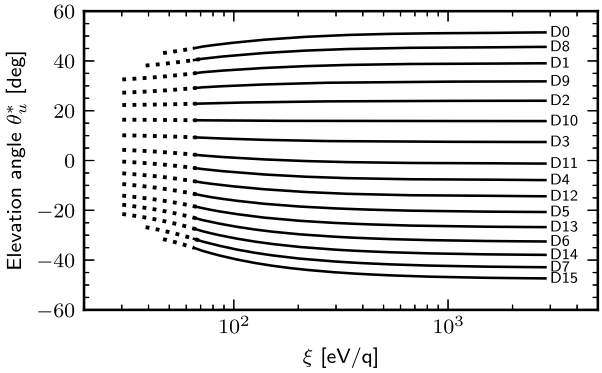

Fig. 18 The average elevation angle θ_u vs. energy. D_n indicates the angular bin number. Below 60 eV/q, the elevation angles are only weakly constrained by calibration data

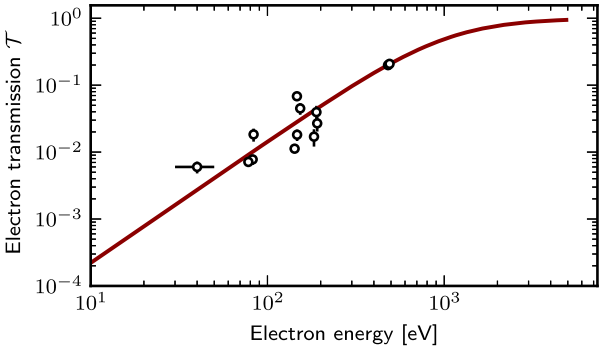

Fig. 19 Measured electron transmission efficiency $\mathcal{T}$ with magnet switched on (open circles). An empirical model for the whole energy range (solid line) is shown

corrected for programmatic reasons. The offset voltages result in a mismatch between ΔV_{defl} and ξ at low energies, and consequently the elevation angle θ being only approximately energy independent. Figure 18 shows how the actual average viewing direction θ_u^* deviates from the values in Table 3 at low energies. Numerically, the actual viewing direction θ_u^* can be approximated for energies above 60 eV/q by

$$\theta_u^*(\xi) \approx \frac{\theta_u(\xi + 2) + 300}{\xi + 30}, \tag{20}$$

where ξ is the energy setting of the electrostatic analyser in units of [eV/q] and θ_u is the nominal angle in degrees tabulated in Table 3. Below 60 eV/q this approximation is not constrained by data and should not be used.

4.5 Electron Suppression

The magnetic electron suppression system is characterised by its transmission efficiency $\mathcal{T}$, which represents the ratio of electrons passing to electrons entering the system. Since the magnetic field strength within the suppression magnet is constant, its efficiency decreases as the electron energy increases. The transmission efficiency (Fig. 19) was experimentally determined[5] by measuring the time-of-flight start count rate for different electron energies

[5]The transmission efficiency was also estimated from ion-optical simulations. The model matches well with experimental data (Canu-Blot 2024, Fig. 3.21).

Table 4 Approximate mass groups

Mass group γ $-m/q$	Representative species	Mass bin range m_b
< 1	e^-	0–5
1	H^-	6–11
2	H_2^-	12–16
4	(He^-)[1]	17–22
8	n/a	23–30
≈ 16	O^-, OH^-	31–50
≈ 28	Si-group	51–63

[1] He^- is meta-stable (Schmidt et al. 2012)

E while switching the magnet on and off. The data were empirically fitted with a function that approaches zero as the electron energy decreases (indicating complete suppression) and approaches unity as the electron energy increases to infinity (indicating no suppression):

$$\mathcal{T}(E) \approx \left[1 + (k_1 E)^{k_2}\right]^{-1}, \tag{21}$$

with E the energy of the electrons in eV and the two fit constants $k_1 = 9.70 \times 10^{-4}$ and $k_2 = -1.82$.

4.6 Mass Response

The mass of a particle is determined from a velocity measurement in the time-of-flight cell. A particle that is detected by the start detector and then by the stop detector results in a coincidence event with an associated time-of-flight t. For a given species, t depends on the energy of the particle in the time-of-flight cell. To remove this dependence on energy, t is converted onboard to an energy-independent mass bin number m_b by multiplying it with a tabulated energy-dependent constant ε_i, where i denotes the energy step number:

$$m_b \equiv \texttt{min}\left(\texttt{floor}(t \cdot \varepsilon_i), 63\right). \tag{22}$$

The `floor()` function returns the largest integer smaller than its argument, and the `min()` function returns the smaller of its two arguments. The calculated value for m_b is guaranteed to be in the range of 0 to 63. The highest mass bin number 63 is special: it contains all events that without the `min()` function would have resulted in a mass bin number of 63 or larger. For each measured time-of-flight event, the element of the data mass matrix corresponding to the mass bin number m_b is incremented by one.

For first-order mass discrimination and provided that each mass group contributes about equally to the signal, it is sufficient to divide the mass bins into groups according to Table 4. To obtain better mass separation, or for the case where the contributions of the different species to the spectrum are very unequal, a more powerful method for mass discrimination is needed. In this case, the measured mass spectrum is interpreted as a vector $\mathbf{M}$ with 64 elements corresponding to the 64 mass bins in the data matrix. The vector $\mathbf{M}$ is then interpreted as a linear combination of calibrated response vectors $\mathbf{M}_\gamma$, where γ corresponds to

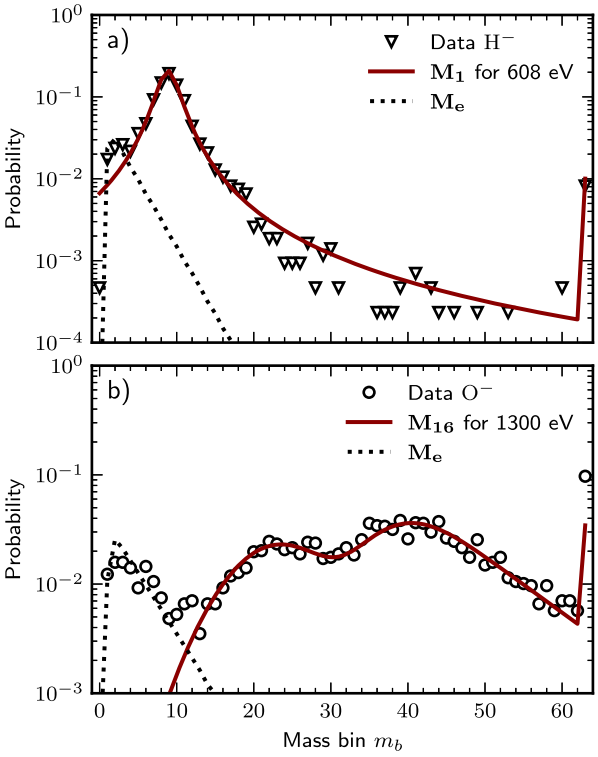

Fig. 20 Example mass response vectors a) $\mathbf{M_1}$ for negative hydrogen ions at 608 eV/q and b) $\mathbf{M_{16}}$ for negative oxygen ions at 1300 eV/q. An electron peak $\mathbf{M_e}$ is visible for both cases. The abscissa denotes mass bin numbers as reported in the telemetry. Data are shown as open circles, smooth empirical functions fitted to the data are shown as solid and dashed lines. The large values in mass bin 63 are due to the processing scheme used

the species and the factor n_γ is larger or equal to zero:

$$\mathbf{M} = \sum_{\gamma} n_\gamma \, \mathbf{M}_\gamma \, . \tag{23}$$

The components of the response vectors $\mathbf{M}_\gamma$ represent the probability of detecting a particle of mass γ in a specific mass bin. n_γ then describes the contribution of each mass response vector to the measured spectrum. The calibrated response vectors were determined for e^-, H^- and O^-.

4.6.1 Hydrogen

From the experimental data, the 64 components of the response vector $\mathbf{M_1}$ for hydrogen ions (Fig. 20a) can be mathematically expressed as

$$\mathrm{M}_{1,m_b} = k_1 \left[\frac{\alpha_1 \, \gamma_1^2}{(m_b - \beta_1)^2 + \gamma_1^2} + \frac{\varepsilon_1^2}{(m_b - \delta_1)^2 + \varepsilon_1^2} \right], \tag{24}$$

$$\mathrm{M}_{1,63} = \sum_{b=63}^{\infty} \mathrm{M}_{1,\mathrm{b}} \, , \tag{25}$$

where k_1 normalises $\mathbf{M_1}$ to unity and m_b is the mass bin number in the range from 0 to 62. The coefficients α_1, β_1, γ_1, δ_1 and ε_1 are empirically determined during calibration and depend on the absolute value ξ in [eV/q] of the energy setting of the electrostatic analyser. The

specified uncertainties are 1-sigma values assuming no correlation between the coefficients.

$$\alpha_1 = (3.26 \pm 0.38) \cdot \mathrm{e}^{-\xi/(723\pm324)} + (2.87 \pm 0.40) \tag{26}$$

$$\beta_1 = (-2.02 \pm 0.80) \cdot \mathrm{e}^{-\xi/(1977\pm1354)} + (10.31 \pm 0.83) \tag{27}$$

$$\gamma_1 = (-0.86 \pm 0.12) \cdot \mathrm{e}^{-\xi/(694\pm269)} + (1.92 \pm 0.12) \tag{28}$$

$$\delta_1 = (-6.38 \pm 0.42) \cdot \mathrm{e}^{-\xi/(792\pm139)} + (11.96 \pm 0.42) \tag{29}$$

$$\varepsilon_1 = 1.80 \pm 0.14 \tag{30}$$

4.6.2 Electrons

There are several possible mechanisms for electrons reaching the exit of the electrostatic analyser: ions with an energy that is different from the electrostatic analyser setting may hit structures near the exit of the electrostatic analyser and create secondary electrons. Ultraviolet photons may create photo-electrons on ion-optical elements and electrons with sufficient energy may pass the electron suppression system despite it being switched on. All these electrons are then accelerated towards the time-of-flight cell where they may generate valid time-of-flight coincidence events. After mass binning, these events appear as an energy-dependent mass peak ($\mathbf{M_e}$ in Fig. 20). The 64 components of the response vector $\mathbf{M_e}$ for electrons can be approximated as:

$$\mathrm{M}_{\mathrm{e},m_b} = k_e \cdot \frac{1}{2\,\tau_e} \cdot \exp\left(\frac{\sigma_e^2}{2\tau_e^2} - \frac{m_b - \mu_e}{\tau_e}\right) \cdot \left\{1 + \mathrm{erf}\left[\frac{1}{\sqrt{2}}\left(\frac{m_b - \mu_e}{\sigma_e} - \frac{\sigma_e}{\tau_e}\right)\right]\right\} \tag{31}$$

$$\mathrm{M}_{\mathrm{e},63} = \sum_{b=63}^{\infty} \mathrm{M}_{\mathrm{e,b}}\,, \tag{32}$$

where k_e normalises $\mathbf{M_e}$ to unity and m_b is the mass bin number in the range from 0 to 62, and ξ in [eV/q] is the absolute value of the energy setting of the electrostatic analyser. Again, the coefficients μ_e, σ_e and τ_e are empirically determined. The specified uncertainties are 1-sigma values assuming no correlation between the coefficients.

$$\mu_e = (-0.956 \pm 0.053) \cdot \mathrm{e}^{-\xi/(366\pm43.6)} + (1.046 \pm 0.06) \tag{33}$$

$$\sigma_e = (1.18 \pm 0.16) \cdot 10^{-7}\xi^2 - (3.59 \pm 0.39) \cdot 10^{-4}\xi + (0.584 \pm 0.013) \tag{34}$$

$$\tau_e = (5.39 \pm 1.11) \cdot 10^{-7}\xi^2 + (1.21 \pm 0.14) \cdot 10^{-3}\xi + (1.440 \pm 0.027) \tag{35}$$

The high fluxes of electrons observed at the lunar surface contrast with the weak electron fluxes produced by the NIOS (see Fig. 10). Therefore, for higher accuracy an improved response vector $\mathbf{M_e}$ for electrons is derived from in-flight data, for which electrons are the dominant species observed for sky-looking directions. The time-of-flight response to electrons is approximated by an exponentially-modified Gaussian with a non-trivial energy dependence (Fig. 21). The components of the improved response vector $\mathbf{M_e}$ for electrons are listed in Table 5, with their uncertainty in Table 6.

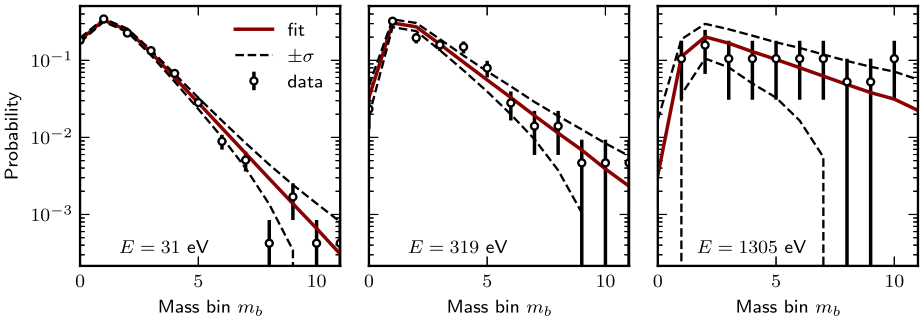

Fig. 21 Energy dependent model of the electron response $\mathbf{M_e}$ derived from in-flight data. The solid lines represent the best estimate, while the dashed contours represent the $\pm 1\sigma$ confidence interval

4.6.3 Oxygen

The oxygen ion signature in the mass spectrum (Fig. 20b) has a more complicated shape than the response for hydrogen ions because heavy ions are able to efficiently create hydrogen recoils from the time-of-flight start surface. These hydrogen recoils originate from water absorbed on the tungsten start surface. Due to the incident oxygen ions being much heavier than the hydrogen recoils, the hydrogen recoils R (Eq. (37)) are faster in the time-of-flight cell than the scattered oxygen atoms S (Eq. (38)). This results in a distinct two-peak shape in the time-of-flight spectrum. The 64 components of the response vector $\mathbf{M_{16}}$ for oxygen ions can be empirically expressed as

$$\mathrm{M}_{16,m_b} = k_{16}\ (R + S)\ , \tag{36}$$

$$R = \exp\left[-\frac{(m_b - 0.667\,\mu_{16})^2}{2\rho_{16}^2}\right], \tag{37}$$

$$S = \frac{A_{16}}{2\,\tau_{16}} \cdot \exp\left(\frac{\sigma_{16}^2}{2\tau_{16}^2} - \frac{m_b - \mu_{16}}{\tau_{16}}\right), \cdot \left\{1 + \mathrm{erf}\left[\frac{1}{\sqrt{2}}\left(\frac{m_b - \mu_{16}}{\sigma_{16}} - \frac{\sigma_{16}}{\tau_{16}}\right)\right]\right\}, \tag{38}$$

$$\mathrm{M}_{16,63} = \sum_{b=63}^{\infty} \mathrm{M}_{16,\mathrm{b}}\,, \tag{39}$$

where similar to the response for hydrogen, k_{16} normalises $\mathbf{M_{16}}$ to unity and m_b is the mass bin number in the range from 0 to 62. The coefficients A_{16}, ρ_{16}, μ_{16}, σ_{16} and τ_{16} are empirically determined and depend partially on the absolute value ξ in [eV/q] of the energy setting of the electrostatic analyser:

$$A_{16} = 33.5 \pm 1.2\,, \tag{40}$$

$$\rho_{16} = 5.70 \pm 0.4\,, \tag{41}$$

$$\mu_{16} = 35.0 \pm 1.0\,, \tag{42}$$

Table 5 Electron mass response $\mathbf{M_e}$ for all energies. At each energy, the probability vector along all the 64 mass bins sums up to 1. Only the probability for the first nine mass bins is shown for compactness, with the probabilities in the remaining mass bins summed up in the last column

Energy	Mass bin m_b									
ξ [eV/q]	0	1	2	3	4	5	6	7	8	$\sum_9^{63}$
3	1.97e-1	3.28e-1	2.39e-1	1.20e-1	6.14e-2	2.90e-2	1.32e-2	6.70e-3	3.05e-3	2.94e-3
9	1.76e-1	3.45e-1	2.38e-1	1.28e-1	5.78e-2	2.92e-2	1.31e-2	6.63e-3	2.99e-3	2.84e-3
14	1.87e-1	3.39e-1	2.38e-1	1.24e-1	6.11e-2	2.67e-2	1.26e-2	6.18e-3	2.70e-3	2.43e-3
20	1.91e-1	3.25e-1	2.43e-1	1.32e-1	5.79e-2	2.73e-2	1.29e-2	6.06e-3	2.96e-3	2.44e-3
25.4	1.92e-1	3.28e-1	2.43e-1	1.25e-1	5.93e-2	2.79e-2	1.31e-2	6.17e-3	3.01e-3	2.47e-3
31.0	1.91e-1	3.32e-1	2.43e-1	1.24e-1	5.85e-2	2.75e-2	1.24e-2	6.30e-3	2.96e-3	2.62e-3
36.6	1.89e-1	3.18e-1	2.51e-1	1.28e-1	6.04e-2	2.83e-2	1.33e-2	5.97e-3	3.04e-3	2.68e-3
42.2	1.69e-1	3.39e-1	2.52e-1	1.27e-1	5.76e-2	2.93e-2	1.37e-2	6.43e-3	2.90e-3	2.78e-3
47.8	1.67e-1	3.42e-1	2.42e-1	1.32e-1	6.21e-2	2.80e-2	1.43e-2	6.45e-3	3.29e-3	2.91e-3
53.4	1.64e-1	3.46e-1	2.42e-1	1.31e-1	5.95e-2	2.92e-2	1.49e-2	6.77e-3	3.46e-3	3.08e-3
59.0	1.62e-1	3.30e-1	2.60e-1	1.25e-1	6.19e-2	3.18e-2	1.45e-2	7.13e-3	3.66e-3	3.29e-3
64.5	1.60e-1	3.33e-1	2.49e-1	1.35e-1	6.19e-2	3.07e-2	1.52e-2	7.84e-3	3.59e-3	3.53e-3
70.6	1.58e-1	3.36e-1	2.48e-1	1.29e-1	6.45e-2	3.22e-2	1.67e-2	7.69e-3	3.84e-3	3.82e-3
77.4	1.56e-1	3.39e-1	2.47e-1	1.29e-1	6.46e-2	3.25e-2	1.63e-2	8.20e-3	4.12e-3	4.16e-3
85.1	1.53e-1	3.22e-1	2.55e-1	1.33e-1	6.75e-2	3.42e-2	1.73e-2	8.40e-3	4.62e-3	4.75e-3
93.6	1.33e-1	3.42e-1	2.53e-1	1.33e-1	6.49e-2	3.60e-2	1.84e-2	8.99e-3	4.98e-3	5.20e-3
103	1.30e-1	3.46e-1	2.41e-1	1.37e-1	6.77e-2	3.78e-2	1.86e-2	1.04e-2	5.13e-3	5.91e-3
113	1.27e-1	3.29e-1	2.60e-1	1.31e-1	7.06e-2	3.97e-2	1.97e-2	1.06e-2	5.97e-3	6.42e-3
125	1.23e-1	3.33e-1	2.48e-1	1.36e-1	7.36e-2	3.99e-2	2.25e-2	1.12e-2	6.09e-3	7.19e-3
138	1.18e-1	3.37e-1	2.36e-1	1.41e-1	7.67e-2	4.17e-2	2.27e-2	1.23e-2	6.70e-3	7.99e-3
153	9.66e-2	3.37e-1	2.56e-1	1.35e-1	7.99e-2	4.35e-2	2.37e-2	1.23e-2	7.32e-3	8.78e-3
170	9.12e-2	3.41e-1	2.45e-1	1.47e-1	7.63e-2	4.32e-2	2.57e-2	1.34e-2	7.94e-3	9.54e-3
188	8.54e-2	3.24e-1	2.55e-1	1.46e-1	8.65e-2	4.49e-2	2.54e-2	1.44e-2	8.16e-3	1.07e-2
209	7.93e-2	3.28e-1	2.44e-1	1.52e-1	8.57e-2	4.84e-2	2.73e-2	1.54e-2	8.73e-3	1.13e-2
232	5.89e-2	3.25e-1	2.68e-1	1.44e-1	8.89e-2	4.76e-2	2.93e-2	1.57e-2	9.67e-3	1.25e-2
258	5.26e-2	3.08e-1	2.80e-1	1.50e-1	8.76e-2	5.11e-2	3.14e-2	1.67e-2	9.77e-3	1.37e-2
286	4.60e-2	3.15e-1	2.67e-1	1.56e-1	9.06e-2	5.27e-2	2.90e-2	1.85e-2	1.08e-2	1.50e-2
318	2.87e-2	3.09e-1	2.78e-1	1.53e-1	9.74e-2	5.34e-2	3.40e-2	1.97e-2	1.08e-2	1.64e-2
354	2.28e-2	2.92e-1	2.89e-1	1.58e-1	9.50e-2	5.71e-2	3.63e-2	1.98e-2	1.19e-2	1.80e-2
394	1.72e-2	3.02e-1	2.72e-1	1.54e-1	1.02e-1	6.11e-2	3.66e-2	2.20e-2	1.32e-2	1.97e-2
439	6.80e-3	2.91e-1	2.65e-1	1.75e-1	1.05e-1	5.91e-2	3.92e-2	2.20e-2	1.46e-2	2.18e-2
489	4.01e-3	2.73e-1	2.72e-1	1.81e-1	1.02e-1	6.35e-2	3.96e-2	2.47e-2	1.64e-2	2.45e-2
545	2.28e-3	2.51e-1	2.79e-1	1.75e-1	1.09e-1	6.86e-2	4.01e-2	2.80e-2	1.75e-2	2.95e-2
607	4.14e-4	2.56e-1	2.55e-1	1.68e-1	1.18e-1	6.96e-2	4.90e-2	2.89e-2	2.04e-2	3.51e-2
677	2.86e-4	2.29e-1	2.58e-1	1.72e-1	1.14e-1	7.60e-2	5.06e-2	3.37e-2	2.24e-2	4.47e-2
755	7.70e-5	2.00e-1	2.58e-1	1.62e-1	1.23e-1	8.30e-2	5.20e-2	3.95e-2	2.67e-2	5.62e-2
842	1.49e-4	1.70e-1	2.37e-1	1.83e-1	1.17e-1	8.35e-2	5.97e-2	4.62e-2	2.95e-2	7.41e-2
939	3.99e-4	1.42e-1	2.33e-1	1.70e-1	1.24e-1	9.00e-2	6.56e-2	4.78e-2	3.19e-2	9.71e-2
1050	4.66e-4	1.41e-1	2.02e-1	1.69e-1	1.15e-1	9.60e-2	6.50e-2	5.45e-2	3.69e-2	1.21e-1

Table 5 (*Continued*)

Energy	Mass bin m_b									
ξ [eV/q]	0	1	2	3	4	5	6	7	8	$\sum_9^{63}$
1170	1.24e-3	1.16e-1	1.98e-1	1.55e-1	1.20e-1	9.26e-2	7.16e-2	5.53e-2	4.28e-2	1.47e-1
1300	1.31e-3	9.76e-2	1.98e-1	1.58e-1	1.10e-1	9.75e-2	7.55e-2	5.27e-2	4.67e-2	1.62e-1
1460	2.19e-3	8.22e-2	2.04e-1	1.49e-1	1.18e-1	1.03e-1	7.14e-2	5.64e-2	4.95e-2	1.65e-1
1620	3.11e-3	9.09e-2	1.93e-1	1.61e-1	1.25e-1	9.63e-2	7.45e-2	5.77e-2	4.47e-2	1.55e-1
1810	2.18e-3	7.86e-2	2.11e-1	1.58e-1	1.38e-1	9.20e-2	8.01e-2	6.00e-2	4.00e-2	1.40e-1
2020	2.08e-3	6.04e-2	2.33e-1	1.77e-1	1.33e-1	9.93e-2	8.30e-2	5.31e-2	3.97e-2	1.19e-1
2260	1.24e-3	5.60e-2	2.29e-1	1.98e-1	1.26e-1	1.08e-1	7.79e-2	5.62e-2	4.06e-2	1.07e-1
2520	2.97e-4	2.19e-2	2.24e-1	1.85e-1	1.59e-1	1.00e-1	8.60e-2	6.18e-2	3.90e-2	1.22e-1
2820	6.73e-4	1.09e-2	1.60e-1	1.69e-1	1.37e-1	1.24e-1	8.17e-2	6.44e-2	5.83e-2	1.94e-1

$$\sigma_{16} = 4.67 \pm 0.19\,, \tag{43}$$

$$\tau_{16} = (3.32 \pm 2.70) \cdot \mathrm{e}^{-\xi/(110\pm105)} + (8.46 \pm 0.40)\,. \tag{44}$$

Excellent agreement with the measured response functions for the ASAN instrument (Wieser et al. 2020) which uses the same geometry for the time-of-flight cell was achieved. Decomposition of a measured spectrum into its components can be done using maximum likelihood fitting methods (e.g. Laurence and Chromy 2010).

4.7 Particle Detection

4.7.1 Detector Bias

We empirically established the relationship between the detector bias voltage and the rate at which particles are detected, as shown in Fig. 22. A bias voltage of 3170 V was selected as the best compromise between maximizing detection efficiency and minimizing voltage. The same bias is applied to both the start and stop detectors.

4.7.2 Detection Probabilities

The probability of detecting a particle of species γ is generally defined by the instrument response function $\mathcal{R}_\gamma$ (Sect. 4.1.2). It is useful to define the average detection probability η as the average of the response function over the region where the function is non-zero

$$\eta_\gamma(\mathbf{u}) \equiv \frac{\int \mathcal{R}_\gamma(\mathbf{u}, \mathbf{v})\, d\mathbf{v}}{\int \mathcal{R}_0(\mathbf{u}, \mathbf{v})\, d\mathbf{v}}\,. \tag{45}$$

We define a time-of-flight start or stop event as a successful detection of a particle at the start or stop detector, respectively. A coincidence event is defined as a start event followed by a stop event combined with a successful measurement of a time-of-flight. In a time-of-flight system, the average detection probabilities can be directly obtained from data measured in-flight (Funsten et al. 2005). Therefore, for an individual measurement setting $\mathbf{u}$, we obtain the average detection probabilities $\eta(\mathbf{u})$ from the number of coincidence events $\mathcal{C}_{\mathrm{coinc}}$, start

Table 6 Uncertainty ($\pm 1\sigma$) in the electron mass response $\mathbf{M_e}$ shown in Table 5 for all energies

Energy	Mass bin m_b									
ξ [eV/q]	0	1	2	3	4	5	6	7	8	$\sum_9^{63}$
3	5.11e-3	4.89e-3	3.32e-3	2.36e-3	1.26e-3	9.09e-4	6.24e-4	4.33e-4	2.52e-4	1.76e-3
9	4.30e-3	5.34e-3	2.88e-3	2.16e-3	1.08e-3	8.35e-4	5.51e-4	3.72e-4	2.12e-4	1.70e-3
14	3.57e-3	4.31e-3	2.26e-3	1.95e-3	1.14e-3	7.64e-4	5.25e-4	3.46e-4	1.92e-4	1.46e-3
20	2.69e-3	3.18e-3	1.82e-3	1.61e-3	6.88e-4	4.89e-4	3.53e-4	2.30e-4	1.45e-4	1.46e-3
25.4	2.94e-3	3.63e-3	2.08e-3	1.76e-3	8.05e-4	5.58e-4	3.99e-4	2.59e-4	1.63e-4	1.48e-3
31.0	2.79e-3	3.48e-3	1.98e-3	1.60e-3	7.37e-4	5.18e-4	3.51e-4	2.43e-4	1.47e-4	1.57e-3
36.6	2.39e-3	2.94e-3	1.68e-3	1.37e-3	6.16e-4	4.34e-4	3.09e-4	1.91e-4	1.24e-4	1.61e-3
42.2	2.17e-3	2.91e-3	1.66e-3	1.26e-3	5.53e-4	4.20e-4	2.98e-4	1.92e-4	1.10e-4	1.67e-3
47.8	2.26e-3	3.08e-3	1.74e-3	1.36e-3	6.30e-4	4.31e-4	3.26e-4	2.01e-4	1.30e-4	1.71e-3
53.4	2.44e-3	3.31e-3	1.94e-3	1.41e-3	6.34e-4	4.70e-4	3.58e-4	2.21e-4	1.44e-4	1.81e-3
59.0	2.59e-3	3.39e-3	2.15e-3	1.36e-3	6.56e-4	5.17e-4	3.54e-4	2.36e-4	1.54e-4	1.92e-3
64.5	2.65e-3	3.44e-3	2.11e-3	1.42e-3	6.40e-4	4.89e-4	3.61e-4	2.53e-4	1.48e-4	2.05e-3
70.6	2.62e-3	3.38e-3	2.12e-3	1.29e-3	6.21e-4	4.80e-4	3.75e-4	2.36e-4	1.49e-4	2.21e-3
77.4	2.51e-3	3.24e-3	2.10e-3	1.18e-3	5.89e-4	4.61e-4	3.43e-4	2.33e-4	1.49e-4	2.35e-3
85.1	2.38e-3	3.10e-3	2.09e-3	1.18e-3	6.00e-4	4.68e-4	3.49e-4	2.27e-4	1.57e-4	2.72e-3
93.6	2.27e-3	3.34e-3	2.21e-3	1.17e-3	6.10e-4	5.11e-4	3.80e-4	2.48e-4	1.72e-4	2.95e-3
103	2.38e-3	3.57e-3	2.33e-3	1.28e-3	6.83e-4	5.76e-4	4.10e-4	3.03e-4	1.88e-4	3.33e-3
113	2.59e-3	3.83e-3	2.70e-3	1.27e-3	7.50e-4	6.42e-4	4.60e-4	3.27e-4	2.30e-4	3.52e-3
125	2.82e-3	4.07e-3	2.78e-3	1.35e-3	7.92e-4	6.52e-4	5.35e-4	3.57e-4	2.42e-4	3.92e-3
138	2.99e-3	4.19e-3	2.75e-3	1.39e-3	8.02e-4	6.69e-4	5.28e-4	3.83e-4	2.62e-4	4.33e-3
153	2.93e-3	4.41e-3	2.89e-3	1.26e-3	7.81e-4	6.59e-4	5.26e-4	3.64e-4	2.70e-4	4.73e-3
170	2.83e-3	4.25e-3	2.66e-3	1.27e-3	6.98e-4	6.03e-4	5.23e-4	3.65e-4	2.73e-4	5.05e-3
188	2.64e-3	4.10e-3	2.60e-3	1.19e-3	7.50e-4	6.11e-4	5.01e-4	3.77e-4	2.68e-4	5.64e-3
209	2.52e-3	4.19e-3	2.57e-3	1.25e-3	7.74e-4	6.85e-4	5.63e-4	4.24e-4	3.01e-4	5.97e-3
232	2.47e-3	4.85e-3	3.10e-3	1.28e-3	8.91e-4	7.47e-4	6.65e-4	4.73e-4	3.65e-4	6.55e-3
258	2.70e-3	5.43e-3	3.65e-3	1.47e-3	9.45e-4	8.57e-4	7.71e-4	5.52e-4	4.03e-4	7.19e-3
286	2.91e-3	5.92e-3	3.92e-3	1.64e-3	1.02e-3	9.35e-4	7.44e-4	6.30e-4	4.63e-4	7.72e-3
318	2.62e-3	6.42e-3	4.35e-3	1.68e-3	1.08e-3	9.21e-4	8.62e-4	6.79e-4	4.70e-4	8.44e-3
354	2.43e-3	6.46e-3	4.66e-3	1.72e-3	1.02e-3	9.54e-4	9.06e-4	6.73e-4	5.10e-4	9.19e-3
394	2.18e-3	6.28e-3	4.46e-3	1.63e-3	1.05e-3	1.01e-3	9.12e-4	7.43e-4	5.66e-4	9.86e-3
439	1.50e-3	6.58e-3	4.56e-3	1.86e-3	1.13e-3	1.06e-3	1.05e-3	7.98e-4	6.68e-4	1.06e-2
489	1.42e-3	7.28e-3	5.21e-3	2.04e-3	1.19e-3	1.24e-3	1.17e-3	9.83e-4	8.31e-4	1.18e-2
545	1.29e-3	8.29e-3	6.17e-3	2.28e-3	1.34e-3	1.42e-3	1.26e-3	1.19e-3	9.55e-4	1.41e-2
607	4.64e-4	9.02e-3	6.30e-3	2.56e-3	1.47e-3	1.39e-3	1.52e-3	1.25e-3	1.13e-3	1.61e-2
677	4.24e-4	9.70e-3	7.07e-3	2.95e-3	1.44e-3	1.41e-3	1.47e-3	1.37e-3	1.19e-3	2.00e-2
755	1.85e-4	1.02e-2	7.76e-3	3.14e-3	1.59e-3	1.38e-3	1.38e-3	1.49e-3	1.35e-3	2.39e-2
842	3.36e-4	1.06e-2	8.06e-3	4.13e-3	1.61e-3	1.24e-3	1.43e-3	1.66e-3	1.44e-3	3.04e-2
939	7.62e-4	1.11e-2	9.24e-3	4.67e-3	2.03e-3	1.26e-3	1.52e-3	1.72e-3	1.57e-3	3.83e-2
1050	9.04e-4	1.19e-2	9.59e-3	5.86e-3	2.43e-3	1.38e-3	1.40e-3	1.91e-3	1.85e-3	4.48e-2
1170	1.88e-3	1.24e-2	1.10e-2	6.82e-3	3.44e-3	1.61e-3	1.37e-3	1.77e-3	2.04e-3	5.36e-2

Table 6 (*Continued*)

Energy	Mass bin m_b									
ξ [eV/q]	0	1	2	3	4	5	6	7	8	$\sum_9^{63}$
1300	1.93e-3	1.21e-2	1.22e-2	8.09e-3	3.88e-3	2.14e-3	1.45e-3	1.60e-3	2.14e-3	5.69e-2
1460	2.74e-3	1.11e-2	1.35e-2	8.46e-3	4.86e-3	2.69e-3	1.46e-3	1.66e-3	2.25e-3	5.67e-2
1620	3.49e-3	1.18e-2	1.35e-2	9.68e-3	5.57e-3	2.78e-3	1.76e-3	1.97e-3	2.30e-3	5.45e-2
1810	2.73e-3	1.18e-2	1.75e-2	1.04e-2	7.02e-3	3.06e-3	2.29e-3	2.58e-3	2.56e-3	5.22e-2
2020	2.83e-3	1.36e-2	2.33e-2	1.28e-2	7.36e-3	3.62e-3	3.12e-3	3.19e-3	3.44e-3	4.64e-2
2260	2.26e-3	1.74e-2	2.53e-2	1.56e-2	7.14e-3	4.00e-3	3.42e-3	4.04e-3	4.27e-3	4.26e-2
2520	1.15e-3	1.71e-2	2.76e-2	1.65e-2	9.57e-3	3.51e-3	3.41e-3	4.36e-3	4.09e-3	4.82e-2
2820	2.25e-3	1.45e-2	3.48e-2	2.47e-2	1.54e-2	9.22e-3	4.02e-3	3.88e-3	5.60e-3	6.50e-2

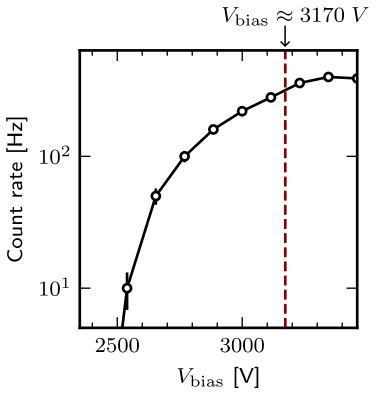

Fig. 22 Empirical relationship between the bias voltage V_{bias} across the start detector and the detection rate. Dots represent observations, with vertical lines indicating counting statistical uncertainties ($\pm\sigma$). The vertical dashed line marks the bias voltage used in the flight model

events $\mathcal{C}_{\text{start}}$, and stop events $\mathcal{C}_{\text{stop}}$ as

$$\eta_{start}\left(\mathbf{u}\right) = \frac{\mathcal{C}_{\text{coinc}}\left(\mathbf{u}\right)}{\mathcal{C}_{\text{stop}}\left(\mathbf{u}\right)}\,, \tag{46}$$

$$\eta_{\text{stop}}\left(\mathbf{u}\right) = \frac{\mathcal{C}_{\text{coinc}}\left(\mathbf{u}\right)}{\mathcal{C}_{\text{start}}\left(\mathbf{u}\right)}\,. \tag{47}$$

As a time-of-flight coincidence event requires both start and stop events to be present, the probability of getting a coincidence event is expressed by

$$\eta_{\text{coinc}} = \eta_{\text{start}}\eta_{\text{stop}}\,. \tag{48}$$

All detection probabilities are assumed to depend only on the energy and the mass of the particle species that generate the detection events. Figure 23 and Table 7 show the average start and stop detection probabilities for H^-, O^-, and e^- across the energy range of the instrument. The start detection probability for all species shows large variations with respect to the energy, most likely due to ion-optical effects, such as the focusing of the particles onto the time-of-flight start surface.

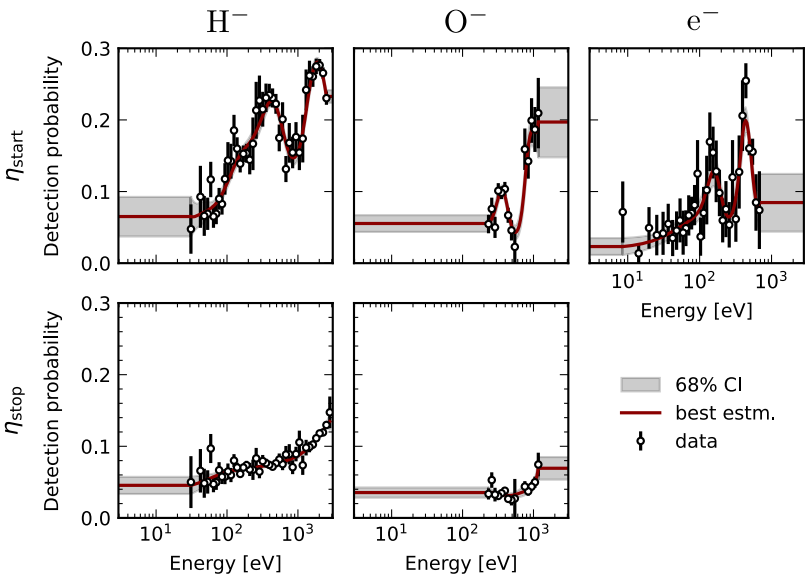

Fig. 23 Detection probabilities for H^-, O^- and e^-. Both start and stop detection probabilities are given for ions, whereas only the start detection probability is given for electrons. The black-circled points are the data, the solid lines are the best estimates of the detection probabilities, and the grey shaded area shows the 68% confidence interval. The detection probabilities are not constrained at all energies due to limitations in the available data. The probabilities at missing energies are estimated from the nearest energy with data

5 Geometric Factor

When exposed to a flux of particles, generally defined by a particle phase space density function f, a particle instrument reports a number of counts $\mathcal{C}$ per integration time period τ. The geometric factor $\mathcal{GF}$ relates the two: it allows to estimate through observation of an instrument-dependent quantity, that is the count rate, the original phase space density of the particle species of interest. This section quantifies the geometric factor from experimental data, using a calibration beam with an energy distribution that is similar to or broader than the energy response of the instrument.

5.1 From Count Rate to Phase Space Density

Equation (9) gives the relation between the observed count rate and the external particle phase space density. Assuming that the phase space density does not possess any structure smaller than the instrument response function (similar to the differential behaviour of Vasyliunas (1971, p. 80)), this equation can be rewritten as:

$$\frac{\mathcal{C}(\mathbf{u})}{\tau} = f(\mathbf{u}) \underbrace{\mathbf{A}(\mathbf{u}) \cdot \int_{\mathbf{v}} \mathbf{v}\mathcal{R}(\mathbf{u},\mathbf{v})\, d\mathbf{v}}_{\text{Instrument-related terms}}. \tag{49}$$

Note that the phase space density function is evaluated at $\mathbf{u}$, indicating that the observation $\mathcal{C}(\mathbf{u})$ provides the most accurate estimate of the density function at the point $\mathbf{v} = \mathbf{u}$ in velocity space. The under-braced term in Eq. (49), which contains only instrument-specific quantities, forms the basis for defining the geometric factor.

Table 7 Detection probabilities as shown in Fig. 23. The 68% confidence intervals shown in Fig. 23 are simplified to a $\pm 1\sigma$ interval in this table

Energy	H^-				O^-				e^-	
ξ [eV/q]	start	σ_{start}	stop	σ_{stop}	start	σ_{start}	stop	σ_{stop}	start	σ_{start}
3	6.60e-2	2.72e-2	4.53e-2	1.21e-2	5.53e-2	1.20e-2	3.54e-2	7.11e-3	2.29e-2	1.12e-2
9	6.60e-2	2.72e-2	4.53e-2	1.21e-2	5.53e-2	1.20e-2	3.54e-2	7.11e-3	2.29e-2	1.12e-2
14	6.60e-2	2.72e-2	4.53e-2	1.21e-2	5.53e-2	1.20e-2	3.54e-2	7.11e-3	2.60e-2	9.71e-3
20	6.60e-2	2.72e-2	4.53e-2	1.21e-2	5.53e-2	1.20e-2	3.54e-2	7.11e-3	2.95e-2	8.72e-3
25.4	6.60e-2	2.72e-2	4.53e-2	1.21e-2	5.53e-2	1.20e-2	3.54e-2	7.11e-3	3.33e-2	8.24e-3
31.0	6.60e-2	2.72e-2	4.53e-2	1.21e-2	5.53e-2	1.20e-2	3.54e-2	7.11e-3	3.72e-2	8.27e-3
36.6	6.65e-2	1.78e-2	4.75e-2	1.06e-2	5.53e-2	1.20e-2	3.54e-2	7.11e-3	4.10e-2	8.65e-3
42.2	6.93e-2	1.58e-2	4.96e-2	9.23e-3	5.53e-2	1.20e-2	3.54e-2	7.11e-3	4.45e-2	9.13e-3
47.8	7.19e-2	1.45e-2	5.17e-2	7.89e-3	5.53e-2	1.20e-2	3.54e-2	7.11e-3	4.78e-2	9.51e-3
53.4	7.41e-2	1.17e-2	5.37e-2	6.67e-3	5.53e-2	1.20e-2	3.54e-2	7.11e-3	5.08e-2	9.66e-3
59.0	7.66e-2	8.63e-3	5.56e-2	5.57e-3	5.53e-2	1.20e-2	3.54e-2	7.11e-3	5.35e-2	9.59e-3
64.5	7.98e-2	6.94e-3	5.73e-2	4.63e-3	5.53e-2	1.20e-2	3.54e-2	7.11e-3	5.59e-2	9.41e-3
70.6	8.40e-2	6.57e-3	5.90e-2	3.80e-3	5.53e-2	1.20e-2	3.54e-2	7.11e-3	5.85e-2	9.27e-3
77.4	8.95e-2	7.03e-3	6.07e-2	3.15e-3	5.53e-2	1.20e-2	3.54e-2	7.11e-3	6.15e-2	9.46e-3
85.1	9.64e-2	7.49e-3	6.23e-2	2.80e-3	5.53e-2	1.20e-2	3.54e-2	7.11e-3	6.52e-2	1.03e-2
93.6	1.05e-1	7.44e-3	6.37e-2	2.73e-3	5.53e-2	1.20e-2	3.54e-2	7.11e-3	7.02e-2	1.18e-2
103	1.14e-1	6.98e-3	6.50e-2	2.80e-3	5.53e-2	1.20e-2	3.54e-2	7.11e-3	7.75e-2	1.34e-2
114	1.24e-1	6.78e-3	6.59e-2	2.82e-3	5.53e-2	1.20e-2	3.54e-2	7.11e-3	8.84e-2	1.46e-2
126	1.34e-1	7.00e-3	6.66e-2	2.72e-3	5.53e-2	1.20e-2	3.54e-2	7.11e-3	1.03e-1	1.54e-2
139	1.44e-1	7.12e-3	6.71e-2	2.49e-3	5.53e-2	1.20e-2	3.54e-2	7.11e-3	1.18e-1	1.77e-2
154	1.51e-1	6.72e-3	6.76e-2	2.26e-3	5.53e-2	1.20e-2	3.54e-2	7.11e-3	1.28e-1	2.10e-2
170	1.58e-1	6.06e-3	6.81e-2	2.05e-3	5.53e-2	1.20e-2	3.54e-2	7.11e-3	1.24e-1	2.06e-2
189	1.63e-1	6.26e-3	6.87e-2	1.90e-3	5.53e-2	1.20e-2	3.54e-2	7.11e-3	1.06e-1	1.65e-2
209	1.68e-1	7.99e-3	6.93e-2	1.81e-3	5.53e-2	1.20e-2	3.54e-2	7.11e-3	8.44e-2	1.33e-2
232	1.75e-1	9.99e-3	7.00e-2	1.78e-3	5.53e-2	1.20e-2	3.54e-2	7.11e-3	6.86e-2	1.31e-2
258	1.84e-1	1.13e-2	7.07e-2	1.82e-3	6.16e-2	7.70e-3	3.52e-2	4.19e-3	6.42e-2	1.40e-2
287	1.94e-1	1.14e-2	7.15e-2	1.89e-3	7.45e-2	8.50e-3	3.48e-2	2.87e-3	7.09e-2	1.53e-2
319	2.06e-1	1.03e-2	7.23e-2	1.97e-3	9.11e-2	7.22e-3	3.41e-2	2.32e-3	9.10e-2	1.66e-2
355	2.17e-1	8.42e-3	7.32e-2	2.02e-3	1.02e-1	6.42e-3	3.30e-2	1.82e-3	1.29e-1	1.83e-2
395	2.25e-1	7.34e-3	7.40e-2	2.03e-3	9.42e-2	6.54e-3	3.19e-2	2.02e-3	1.77e-1	2.12e-2
440	2.26e-1	7.43e-3	7.50e-2	2.00e-3	7.29e-2	6.39e-3	3.14e-2	2.67e-3	1.99e-1	1.76e-2
490	2.20e-1	7.53e-3	7.60e-2	1.96e-3	5.26e-2	7.97e-3	3.15e-2	3.18e-3	1.74e-1	8.41e-3
545	2.06e-1	7.21e-3	7.71e-2	1.99e-3	4.34e-2	9.11e-3	3.23e-2	3.79e-3	1.25e-1	1.39e-2
608	1.87e-1	7.13e-3	7.83e-2	2.15e-3	4.81e-2	1.03e-2	3.39e-2	4.80e-3	8.64e-2	1.81e-2
678	1.68e-1	7.86e-3	7.96e-2	2.46e-3	6.93e-2	1.27e-2	3.58e-2	5.73e-3	8.40e-2	4.00e-2
755	1.53e-1	8.87e-3	8.13e-2	2.82e-3	1.13e-1	1.71e-2	3.75e-2	5.37e-3	8.40e-2	4.00e-2
842	1.47e-1	9.49e-3	8.32e-2	3.17e-3	1.61e-1	1.89e-2	3.93e-2	4.09e-3	8.40e-2	4.00e-2
940	1.49e-1	9.63e-3	8.54e-2	3.45e-3	1.84e-1	1.99e-2	4.27e-2	4.30e-3	8.40e-2	4.00e-2
1050	1.61e-1	9.37e-3	8.81e-2	3.59e-3	1.84e-1	2.52e-2	5.01e-2	5.82e-3	8.40e-2	4.00e-2

Table 7 (*Continued*)

Energy	H^-				O^-				e^-	
ξ [eV/q]	start	σ_{start}	stop	σ_{stop}	start	σ_{start}	stop	σ_{stop}	start	σ_{start}
1170	1.82e-1	9.00e-3	9.12e-2	3.55e-3	1.97e-1	4.68e-2	6.95e-2	1.59e-2	8.40e-2	4.00e-2
1300	2.12e-1	9.20e-3	9.48e-2	3.32e-3	1.97e-1	4.68e-2	6.95e-2	1.59e-2	8.40e-2	4.00e-2
1460	2.43e-1	9.61e-3	9.90e-2	2.90e-3	1.97e-1	4.68e-2	6.95e-2	1.59e-2	8.40e-2	4.00e-2
1620	2.67e-1	8.58e-3	1.04e-1	2.43e-3	1.97e-1	4.68e-2	6.95e-2	1.59e-2	8.40e-2	4.00e-2
1810	2.80e-1	6.35e-3	1.09e-1	2.14e-3	1.97e-1	4.68e-2	6.95e-2	1.59e-2	8.40e-2	4.00e-2
2020	2.77e-1	5.78e-3	1.16e-1	2.15e-3	1.97e-1	4.68e-2	6.95e-2	1.59e-2	8.40e-2	4.00e-2
2260	2.60e-1	5.97e-3	1.22e-1	2.25e-3	1.97e-1	4.68e-2	6.95e-2	1.59e-2	8.40e-2	4.00e-2
2520	2.33e-1	8.84e-3	1.29e-1	4.06e-3	1.97e-1	4.68e-2	6.95e-2	1.59e-2	8.40e-2	4.00e-2
2820	2.33e-1	8.84e-3	1.35e-1	1.13e-2	1.97e-1	4.68e-2	6.95e-2	1.59e-2	8.40e-2	4.00e-2

5.2 Definition of the Absolute Geometric Factor

A fundamental property of electrostatic instruments[6] is that the relative shape of $\mathcal{R}_0(\mathbf{u}, \mathbf{v})$ is independent of the magnitude of $\mathbf{u}$ (Vasyliunas, 1971, Eq. 12.3.4; Johnstone et al., 1987, p. 801; Kessel et al., 1989, p. 3753):

$$\mathcal{R}_0(\mathbf{u}, \mathbf{v}) = \mathcal{R}_0\left(\mathbf{u}', \mathbf{v}'\right), \tag{50}$$

with $\mathbf{u}' = \mathbf{u}/u$ and $\mathbf{v}' = \mathbf{v}/u$. It follows from Eq. (49) that:

$$\mathbf{A}(\mathbf{u}) \cdot \int \mathbf{v}\mathcal{R}_0(\mathbf{u}, \mathbf{v})\, d\mathbf{v} = u^4 \underbrace{\left[\mathbf{A}(\mathbf{u}) \cdot \int \mathbf{v}'\mathcal{R}_0\left(\mathbf{u}', \mathbf{v}'\right) d\mathbf{v}'\right]}_{\mathcal{GF}_0(\mathbf{u})}. \tag{51}$$

For a particular measurement setting $\mathbf{u}$, the absolute geometric factor $\mathcal{GF}_0$ is a constant of the instrument. It corresponds to the normalised volume of the ideal instrument response function in velocity- or energy-space multiplied by the effective area. We finally give the definition of the absolute geometric factor $\mathcal{GF}_0$ $\left[\mathrm{m}^2\right]$ used in this paper (Wurz et al. 2007, Eq. 3.7):

$$\boxed{\mathcal{GF}_0(\mathbf{u}) \equiv \underbrace{\frac{1}{u^4}}_{[\mathrm{s}^4/\mathrm{m}^4]} \underbrace{\mathbf{A}(\mathbf{u}) \cdot \int \mathbf{v}\mathcal{R}_0(\mathbf{u}, \mathbf{v})\, d\mathbf{v}}_{[\mathrm{m}^6/\mathrm{s}^4]}}. \tag{52}$$

5.2.1 Energy-Independence Property

A direct consequence of the scaling property of $\mathcal{R}_0$ (Eq. (50)) is that the absolute geometric factor depends only on the direction of $\mathbf{u}$ and not its magnitude u. To emphasise this property, Eq. (52) can be rewritten as (Lavraud and Larson 2016, Eq. 8):

$$\mathcal{GF}_0(\mathbf{u}) = \mathcal{GF}_0(k\mathbf{u}), \text{ with } k \in \mathbb{R}^+. \tag{53}$$

[6] We ignore here effects such as detection probabilities, see Sect. 4.7.2.

This property simplifies both the determination and the application of the geometric factor, which only needs to be estimated for different directions of $\mathbf{u}$.

5.2.2 Geometric Factor Including Detection Probabilities

The absolute geometric factor defined in Equation (52) is a purely geometric quantity, based on the ideal response function of the instrument given in Equation (4). In reality, the instrument response function also includes detection probabilities. These detection probabilities depend on various factors, including particle energy, species, and the time of measurement (e.g. detector ageing). From the knowledge of the average detection probability η, obtained independently (Sect. 4.7.2), we can approximate the instrument response as a step function:

$$\mathcal{R}\left(\mathbf{u},\mathbf{v}\right) \approx \eta\left(\mathbf{u}\right)\mathcal{R}_0\left(\mathbf{u},\mathbf{v}\right). \tag{54}$$

It follows that the relation between the absolute geometric factor $\mathcal{GF}_0$ and the geometric factor including efficiencies $\mathcal{GF}$ is approximated as

$$\mathcal{GF}\left(\mathbf{u}\right) \approx \eta\left(\mathbf{u}\right)\mathcal{GF}_0\left(\mathbf{u}\right). \tag{55}$$

5.3 Experimental Determination of the Absolute Geometric Factor

NILS instrument velocity-space measurements are given in instrument-specific coordinates (ξ,α,θ), rather than velocity (Sect. 4.1.2). Therefore, it is convenient to express Eq. (9) in instrument-specific coordinates (Figs. 8 and 11) using the coordinate transformation below:

$$\begin{aligned}
&\begin{cases} v_x = -v\cos\alpha\sin\theta \\ v_y = -v\sin\alpha \\ v_z = v\cos\alpha\cos\theta \end{cases}, \\
&\hat{\mathbf{A}}\cdot\mathbf{v} = v\cos\alpha\cos\theta\,, \\
&d\mathbf{v} = v^2 dv\cos\alpha d\alpha d\theta\,, \\
&v = \sqrt{\frac{2eq\xi}{m}}\,, \\
&dv = \sqrt{\frac{eq}{2m\xi}}d\xi\,.
\end{aligned} \tag{56}$$

The following derivations and results are given for an arbitrary particle species γ. We rewrite Eq. (9) and Eq. (52) using the instrument coordinate system:

$$\begin{aligned}
\frac{\mathcal{C}\left(\mathbf{u}\right)}{\tau} = 2\mathrm{A}\left(\mathbf{u}\right)\kappa\left(\mathbf{u}\right)\left(\frac{eq}{m}\right)^2 \iiint \xi\cos^2\alpha\cos\theta \\
\cdot f\left(\xi,\theta,\alpha\right)\mathcal{R}_\Omega\left(\mathbf{u},\theta,\alpha\right)\ \mathcal{R}_E\left(\mathbf{u},\xi\right)d\theta d\alpha d\xi\,,
\end{aligned} \tag{57}$$

$$\begin{aligned}
\mathcal{GF}\left(\mathbf{u}\right) = \frac{\mathrm{A}\left(\mathbf{u}\right)\kappa\left(\mathbf{u}\right)}{2\xi_u^2}\iiint \xi\cos^2\alpha\cos\theta \\
\cdot\mathcal{R}_\Omega\left(\mathbf{u},\theta,\alpha\right)\ \mathcal{R}_E\left(\mathbf{u},\xi\right)d\theta d\alpha d\xi\,.
\end{aligned} \tag{58}$$

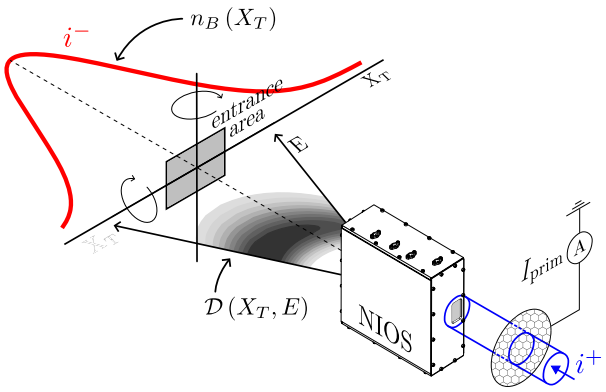

Fig. 24 Negative ions beam profile produced by the NIOS. A parallel positive ion beam i^+ (blue) enters the NIOS and is converted to a divergent negative ion beam with a position dependent number density n_B (red line), with the width of its profile larger than the NILS entrance area (shaded rectangle). The energy of the negative ion beam also depends on the position, as schematized by the gray colormap. The current I_{prim} is picked up from a 90% transparent grid placed in the positive ion beam, allowing to monitor temporal variations in the positive ion beam density entering the NIOS

From Eq. (58), we see that the calculation of the geometric factor is based on the determination of the scaling factor κ, the effective area A, and the angular response function $\mathcal{R}_\Omega$. The energy response $\mathcal{R}_E\,(\mathbf{u}, \xi)$ has been estimated separately in Sect. 4.3 using electron measurements.

5.3.1 The Negative Ion Beam

The estimation of the instrument response is typically achieved using a collimated monoenergetic calibration beam with a known particle phase space density. However, IRF calibration facilities can only generate positively charged ion beams, requiring the use of the NIOS to produce the negative ion beam necessary to calibrate the NILS instrument (Sect. 3). The negative ion beam exiting the NIOS exhibits significant angular and energy spread, characteristics inherent to systems that use charge conversion surfaces (Fig. 24).

We assume that the effective area of the instrument is small compared to the width of the negative ion beam given by the angular spread at any position $\mathbf{x}$ in the calibration chamber. We can therefore model the fraction of the beam entering the instrument by an equivalent parallel and collimated negative ion beam of density $n_B\left[\#/m^3\right]$, direction $\hat{\mathbf{v}}_\mathbf{B}$, and speed distribution $\mathcal{D}_v\,(\mathbf{x}, v)$ (or energy distribution $\mathcal{D}\,(\mathbf{x}, \xi)$). The phase space density $f_B\ \left[\mathrm{s}^3/\mathrm{m}^6\right]$ of this equivalent negative ion beam can be written as:

$$f_B\,(\mathbf{x}, \mathbf{v}, t) \equiv n_B\,(\mathbf{x}, t)\ \underbrace{\delta\left(\frac{\mathbf{v}}{v} - \hat{\mathbf{v}}_\mathbf{B}\,(\mathbf{x})\right)}_{[\mathrm{s}^2\cdot\mathrm{m}^{-2}]}\ \underbrace{\mathcal{D}_v\,(\mathbf{x}, v)}_{[\mathrm{s}\cdot\mathrm{m}^{-1}]}. \tag{59}$$

The angular distribution of the equivalent negative ion beam is modelled by a velocity-normalised 3-dimensional Delta-Dirac distribution. Expressing f_B in the NILS instrument

coordinate system (ξ, θ, α) yields

$$f_B(\mathbf{x}, \xi, \theta, \alpha, t) = n_B(\mathbf{x}, t)\,\delta(\theta - \theta_B(\mathbf{x}))\,\delta(\alpha - \alpha_B(\mathbf{x})) \cdot \underbrace{\left(\frac{m}{eq}\right)^{3/2} \frac{1}{\sqrt{2\xi}\cos\alpha}\mathcal{D}(\mathbf{x}, \xi)}_{[s^3.m^{-3}]}. \tag{60}$$

Assuming that $n_B(\mathbf{x}, t)$ is constant over the integration time of the instrument, we can inject Eq. (60) into Eq. (57) and integrate the result over (θ, α). At a given position $\mathbf{x}$, we obtain the following relation:

$$\frac{\mathcal{C}(\mathbf{u})}{\tau} = \mathrm{A}(\mathbf{u})\, n_B \cos\alpha_B \cos\theta_B \kappa(\mathbf{u})\, \mathcal{R}_\Omega(\mathbf{u}, \theta_B, \alpha_B) \cdot \int \sqrt{\frac{2eq\xi}{m}} \mathcal{R}_E(\mathbf{u}, \xi)\, \mathcal{D}(\xi)\, d\xi, \tag{61}$$

Solving for $\kappa \mathcal{R}_\Omega \mathrm{A}$ finally yields:

$$\boxed{\kappa(\mathbf{u})\, \mathcal{R}_\Omega(\mathbf{u}, \theta_B, \alpha_B)\, \mathrm{A}(\mathbf{u}) = \frac{\mathcal{C}(\mathbf{u})/\tau}{\Lambda(\mathbf{u})\, n_B} [\cos\alpha_B \cos\theta_B]^{-1}}, \tag{62}$$

with $\Lambda(\mathbf{u}) \equiv \int \sqrt{2eq\xi/m}\mathcal{R}_E(\mathbf{u}, \xi)\, \mathcal{D}(\xi)\, d\xi$. The quantity Λ $\left[\mathrm{m/s \cdot q/eV}\right]$ relates to the average speed of the observed beam for one specific measurement. Similarly, Λn_B $\left[1/\left(\mathrm{m}^2 \cdot \mathrm{s}\right) \cdot \mathrm{q/eV}\right]$ is related to the average observed beam number flux. Therefore, similarly to Collinson et al. (2012, Eq. 28), we can scan the instrument response by performing angular scans using a collimated negative ion beam and normalising the observed count rate by the beam number flux. The following sections will be dedicated to the estimation of the negative ion beam number density n_B and energy distribution $\mathcal{D}(\xi)$.

Beam Energy Distribution The estimation of the calibration beam energy distribution $\mathcal{D}$ relies on our previous estimate of the instrument energy response function (Sect. 4.3), which is assumed to be angular-independent. We begin by rewriting Eq. (61) as:

$$\mathcal{C}(\mathbf{u}) = \Psi(\mathbf{u}, \mathbf{v}_B) \int \sqrt{\xi} \mathcal{R}_E(\mathbf{u}, \xi)\, \mathcal{D}(\xi)\, d\xi\,, \tag{63}$$

using $\Psi(\mathbf{u}, \mathbf{v}_B)$ to encapsulate all terms that are independent of the instrument energy setting. The best estimate $\hat{\mathcal{D}}$ of the energy distribution of the beam from the observation $\mathcal{C}$ of the beam $\mathcal{D}$ by the known function $\mathcal{R}_E$ is given by:

$$\hat{\mathcal{D}}(\xi) = \arg\min_{\mathcal{D}(\xi)} \left(\sum_{\mathbf{u}} \left\| \mathcal{C}(\mathbf{u}) - \cancel{\Psi(\mathbf{u}, \mathbf{v}_B)}^{\text{ignored}} \int \sqrt{\xi} \mathcal{R}_E(\mathbf{u}, \xi)\, \mathcal{D}(\xi)\, d\xi \right\| \right). \tag{64}$$

As the term Ψ is constant for each measurement setting, its value does not influence the estimation of $\mathcal{D}$. The discrete sum in Eq. (64) describes the sum over all energy measurements covering the observed beam. The observed counts $\mathcal{C}$ are fitted by an exponentially-modified Gaussian to improve stability of the numerical minimisation. An example of the beam energy distribution retrieval based on the Eq. (64) is shown in Fig. 25. It is important

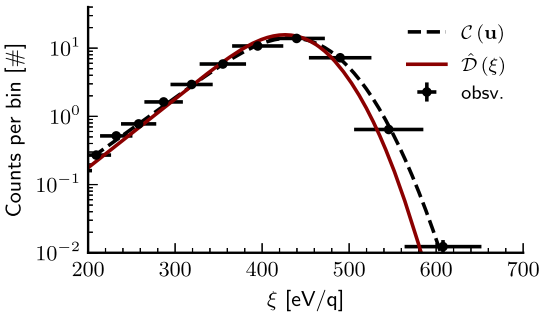

Fig. 25 Negative ion beam energy distribution estimate from an observed energy spectrum using Eq. (64). The black points represent real data, where horizontal error bars indicate the uncertainty on the energy estimate, and vertical bars represent counting errors

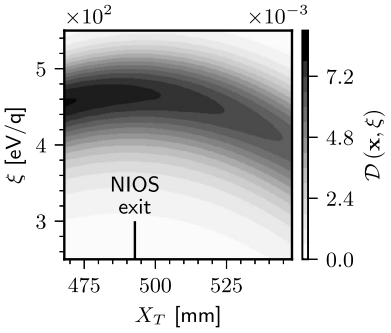

Fig. 26 The energy distribution function $\mathcal{D}$ of the negative ion calibration beam at the entrance of the NILS instrument exhibits a decrease in the average ion beam energy as X_T increases. This decline arises from slower ions experiencing larger deflection before exiting the NIOS

to remember that the retrieval of $\mathcal{D}(\xi)$ must be performed at each instrument position used for calibration as $\mathcal{D}(\mathbf{x}, \xi)$ is a function of the position inside the calibration chamber. Figure 26 shows the complete beam energy distribution $\mathcal{D}(\mathbf{x}, \xi)$ obtained for a 1 keV primary H_2^+ beam.

Beam Number Density We estimate the number density n_B of the negative ion beam by measuring the current density j $\left[\mathrm{A/m^2}\right]$ at the NIOS output using a Faraday cup (Wecker 2024). The current density is assumed to be constant across the effective area of the Faraday cup. Particular attention was paid to eliminating the contribution of electrons to the measurement. It is important to note that the Faraday cup detects all energies and provides an estimate of the energy-integrated current density because it lacks an electrostatic filtering system. To correct for fluctuations in the primary positive ion beam intensity, the measured current density j is normalized by the estimated total intensity of the primary positive ion beam entering the NIOS, denoted I_{prim} [A] (see Fig. 24).

We define the intensity-normalised energy-integrated number flux $\bar{\Phi}$ $\left[\#/\left(\mathrm{m^2 \cdot s \cdot A}\right)\right]$ as:

$$\bar{\Phi}\left(\mathbf{x}, E_{\mathrm{prim}}\right) \equiv \frac{j\left(\mathbf{x}, E_{\mathrm{prim}}\right)}{eq\ I_{\mathrm{prim}}}, \tag{65}$$

with I_{prim} the average best estimate of the total positive ion beam intensity entering the NIOS at the time of the measurement. Using the values of $\bar{\Phi}$ estimated during the NIOS characterisation campaign (Fig. 27, adapted from Wecker 2024, Fig. 2.15) and the beam energy estimated distribution, we can compute the negative ion beam intensity-normalised

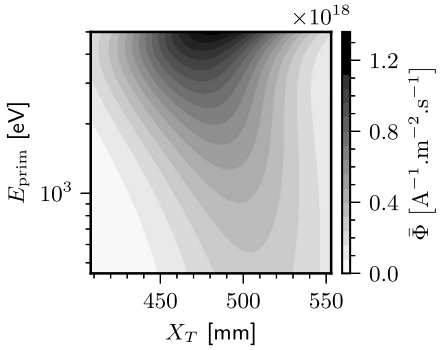

Fig. 27 The negative ion beam intensity depends on the primary positive ion beam energy, species and intensity. It is also non-uniform in space, and thus depends on where it is observed. The intensity of the negative ion beam linearly increases as the primary beam intensity. The data shown are for singly-charged negative ions. As an element of comparison, for a typical primary positive ion beam intensity of 1 nA, the maximum negative ion number density observed corresponds to approximately 1‰ of the solar wind proton density at 1 au

number density $\overline{n}_B$ $\left[\#/\left(\mathrm{m}^3 \cdot \mathrm{A}\right)\right]$:

$$\overline{n}_B\left(\mathbf{x}, E_{\mathrm{prim}}\right) = \bar{\Phi}\left(\mathbf{x}, E_{\mathrm{prim}}\right) \int \hat{\mathcal{D}}\left(\xi\right) \sqrt{\frac{m}{2eq\xi}} d\xi. \tag{66}$$

With knowledge of the intensity of the primary positive ion beam $I_{\mathrm{prim}}\left(t\right)$, which is constantly monitored during the calibration of NILS, we can calculate the number density n_B $\left[\mathrm{m}^{-3}\right]$ using the relation:

$$n_B\left(\mathbf{x}, E_{\mathrm{prim}}, t\right) = I_{\mathrm{prim}}\left(t\right) \overline{n}_B\left(\mathbf{x}, E_{\mathrm{prim}}\right). \tag{67}$$

5.3.2 Integration of $\mathcal{R}$

Using the estimated beam density $n_B(\mathbf{x}, E_{\mathrm{prim}}, t)$ and energy distribution $\mathcal{D}(\mathrm{x}, \xi)$, we can now use Eq. (62) to compute $\kappa \mathcal{R}_\Omega A$ for each measurement setting $\mathbf{u}$ as a function of the angular scan directions (α, θ) (see Fig. 28 for a quantitive example[7]). Combining the expression of $\kappa \mathcal{R}_\Omega A$ from Eq. (62) with Eq. (58) yields:

$$\mathcal{GF}\left(\mathbf{u}\right) = \left[2\xi_u^2 \tau \Lambda\left(\mathbf{u}\right) n_B\right]^{-1} \iiint \mathcal{C}\left(\mathbf{u}\right) \xi \mathcal{R}_E\left(\mathbf{u}, \xi\right) \cos\alpha d\theta d\alpha d\xi\,. \tag{68}$$

We can simplify the Eq. (68) by noting that $\xi_u = \int \xi \mathcal{R}_E\left(\mathbf{u}, \xi\right) d\xi$. Then, by dividing Eq. (68) by the average detection probability η, and transforming the integrals over θ and α by two middle Riemann sums, we finally get the equation used to derive the absolute

[7]The data in Fig. 28, together with the independently determined detection probabilities from Sect. 4.7.2, allows for an independent estimate of the instrument effective area. For a central-looking angular pixel, the estimated value is $A \approx 0.43 \pm 0.20$ cm^2, closely matching the geometric aperture area of 0.316 cm^2 at the entrance of the electrostatic analyzer. This independent verification confirms the validity of the method and assumptions presented in this analysis.

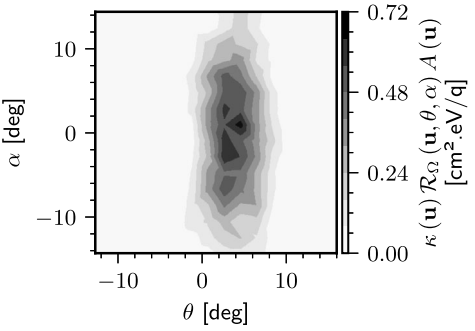

Fig. 28 Angular response function scaled by the effective area, as obtained from the Eq. (62). The data shown are from an angular pixel centred at $\theta = 4°$, observing a beam with a mean energy of 413 eV/q

geometric factor:

$$\boxed{\mathcal{GF}_0(\mathbf{u}) \approx [2\xi_u \tau \Lambda(\mathbf{u}) \eta(\mathbf{u}) \overline{n}_B]^{-1} \sum_i \sum_j \cos\alpha_i \left[\frac{\mathcal{C}(\mathbf{u})}{I_{\text{prim}}} \Delta\Omega\right]_{ij}}, \tag{69}$$

with i and j representing the indices of each angular step (α_i, θ_j) of the angular scan. The resolution in solid angle of the angular scan is written as $\Delta\Omega_{ij} = \Delta\alpha_i \Delta\theta_j$. The variation in the number density of the beam over time is accounted for by the primary current I_{prim}, evaluated as each angular step.

5.3.3 Uncertainty Determination

The geometric factor involves multiple products of the calibration campaign. Consequently, due to uncertainties in the calibration beam characteristics, instrument energy response, and the stochastic nature of counting processes, it is subject to some degree of uncertainty.

The primary sources of uncertainty in the estimation of the geometric factor arise from the stochastic Poisson nature of the observed count number $\mathcal{C}$, the beam density, the detection efficiency η, and the parameter Λ, which encapsulates uncertainties in both the energy response of the instrument and the beam energy spectrum.

By approximating Eq. (69) to a first-order Taylor series expansion, we derive the variance in the estimate of the absolute geometric factor by adding variances of its assumed uncorrelated parameters:

$$\begin{aligned}\mathtt{Var}[\mathcal{GF}_0(\mathbf{u})] \approx \mathcal{GF}_0^2 &\left[\frac{\mathtt{Var}[\Lambda(\mathbf{u})]}{\Lambda(\mathbf{u})^2} + \frac{\mathtt{Var}[\eta(\mathbf{u})]}{\eta(\mathbf{u})^2} + \frac{\mathtt{Var}[\overline{n}_B]}{\overline{n}_B^2}\right] \\ &+ \rho(\mathbf{u})^2 \sum_i^{\alpha_B} \sum_j^{\theta_B} \left[\cos^2\alpha_i \left(\frac{\Delta\Omega}{I_{\text{prim}}}\right)_{ij}^2 \mathtt{Var}[\mathcal{C}(\mathbf{u})]_{ij}\right],\end{aligned} \tag{70}$$

with $\rho(\mathbf{u}) = [2\xi_u \tau \Lambda(\mathbf{u}) \eta(\mathbf{u}) \overline{n}_B]^{-1}$ the angular-independent factor in Eq. (69) and $\mathtt{Var}[\cdot]$ the variance in the variable uncertainty.

The uncertainty in the intensity-normalised beam density is significant, as the negative ion source proved to be sensitive to a number of a priori unknown factors, for example the spatial drifting of the primary ion beam. Its uncertainty is evaluated from the residual of the empirical fit done over the observations of the geometric factor, as detailed in the Sect. 5.3.5.

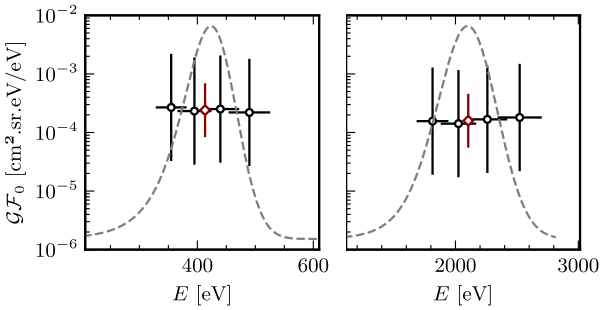

Fig. 29 The absolute geometric factor, as defined in Eq. (69), plotted for four measurement settings adjacent to the energy where the calibration beam is at its peak flux (open circles). The left and right panels show the responses to two calibration beams at different energies. Vertical error bars depict a 68% confidence interval, while horizontal bars indicate the energy resolution. A dashed line is included to illustrate the energy distribution of the calibration beam as derived from Eq. (64). The absolute geometric factor's best estimate $\widehat{\mathcal{GF}_0}$ is shown as open diamond, with vertical bars showing the $\pm 1\sigma$ interval

5.3.4 The Absolute Geometric Factor

As shown in Sect. 5.2, the absolute geometric factor is energy-independent, and therefore should be the same when calculated for all energy bins for a given elevation step. In practice, we run the calculation for energy bins neighbouring the energy where the beam is at its peak flux (Fig. 29). In doing so, we gather a sequence of independent observations of the absolute geometric factor $\mathcal{GF}_0\left(u_i\hat{\mathbf{u}}\right)$ with i the energy bin index and $\hat{\mathbf{u}}$ a unit vector representing the average direction of the measurement. All these observations are aggregated altogether by using an inverse-variance weighting method to finally obtain one single, best estimate $\widehat{\mathcal{GF}_0}$ of the absolute geometric factor for all measurement settings $u\hat{\mathbf{u}}$. The inverse-weighted average is given below:

$$\widehat{\mathcal{GF}_0}\left(\hat{\mathbf{u}}\right) = \sum_i \frac{\mathcal{GF}_0\left(u_i\hat{\mathbf{u}}\right)}{\mathtt{Var}\left[\mathcal{GF}_0\left(u_i\hat{\mathbf{u}}\right)\right]} \mathtt{Var}\left[\widehat{\mathcal{GF}_0}\left(\hat{\mathbf{u}}\right)\right], \tag{71}$$

with its variance:

$$\mathtt{Var}\left[\widehat{\mathcal{GF}_0}\left(\hat{\mathbf{u}}\right)\right] = \left(\sum_i \frac{1}{\mathtt{Var}\left[\mathcal{GF}_0\left(u_i\hat{\mathbf{u}}\right)\right]}\right)^{-1}. \tag{72}$$

The method is depicted in Fig. 29 for two sets of measurements at a different beam energy. The final best estimate has the least variance amongst all observations.

5.3.5 Results and Performance

The absolute geometric factor is estimated from multiple measurements of the negative ion beam at different energies, observed from different elevations. All resulting estimators are shown in Fig. 30, with tabulated values for each of the 16 elevation steps shown in Table 8. An estimate $\mathcal{GF}_0^{\text{gem}}$ based on pure geometrical considerations is shown for comparison. The latter is calculated by simplifying the Eq. (58) for a central-looking pixel, for which the effective area is well-approximated by the entrance slit of the electrostatic analyser, $A \approx$

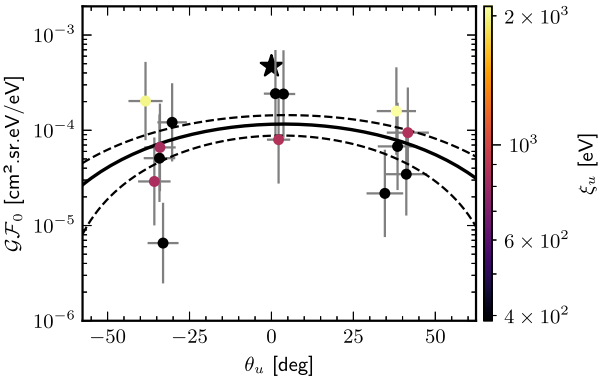

Fig. 30 Angular-dependent absolute geometric factor (solid line) with a 68% confidence interval (dashed line). The vertical error bar on the individual data points shows a 68% confidence interval of the geometric factor estimate. The horizontal error bar shows the size $\Delta\theta$ of the associated angular pixel, as defined in Table 3. The colours indicate the energy-per-charge ξ_u used for each individual measurement. The geometrical estimate $\mathcal{GF}_0^{\text{gem}}$ is shown as a black star

Table 8 The velocity-derived absolute geometric factor $\mathcal{GF}_0$ and the energy-derived absolute geometric factor $\mathbb{GF}_0$, both for the 16 angular bins. A 68% confidence interval is given for each estimate of the velocity-derived absolute geometric factor

Angular bin number D_n	θ_u [deg]	$\mathcal{GF}_0$ 10^{-4} [cm^2 sr eV/eV]	$\mathcal{GF}_0$ 68% C.I. 10^{-4} [cm^2 sr eV/eV]	$\mathbb{GF}_0$ 10^{-4} [cm^2 sr eV/eV]
0	52	0.52	(0.31, 0.86)	1.0
1	39	0.77	(0.53, 1.13)	1.5
2	24	1.0	(0.77, 1.37)	2.0
3	7.4	1.2	(0.91, 1.48)	2.3
4	−7.5	1.1	(0.87, 1.43)	2.2
5	−20	0.97	(0.73, 1.28)	1.9
6	−32	0.76	(0.54, 1.08)	1.5
7	−43	0.55	(0.35, 0.86)	1.1
8	46	0.64	(0.41, 0.99)	1.3
9	32	0.91	(0.65, 1.26)	1.8
10	16	1.1	(0.86, 1.44)	2.2
11	−1.0	1.2	(0.91, 1.46)	2.3
12	−14	1.1	(0.81, 1.36)	2.1
13	−26	0.87	(0.64, 1.18)	1.7
14	−38	0.65	(0.44, 0.97)	1.3
15	−48	0.46	(0.27, 0.76)	0.91

0.316 cm^2. This yields: $\mathcal{GF}_0^{\text{gem}} \equiv (0.85A)/2 \cdot \Delta\Omega \cdot E_{\text{res}}$, with $\Delta\Omega$ the solid angle at half maximum of the angular response for $\theta_u = 0$ (see Table 3), E_{res} the energy resolution, and the factor 0.85 accounting for the transparency of the entrance grid.

The absolute geometric factor is fitted using an empirical cosine-squared function on the average elevation angle. The fit model is presented below:

$$\mathcal{GF}_0(\theta_u) = k_1 \cos^2(\theta_u - k_2) \ , \tag{73}$$

with θ_u the centre in elevation of a measurement and the two fit parameters $k_1 = 1.16 \times 10^{-4}$ cm^2 and $k_2 = 3.70$ deg. The fit residual is following a log-normal distribution of sig-

nificant spread (about a factor of 2), most likely attributed to the beam density fluctuations not accounted for in our model.

An alternative definition of the geometric factor, known as the energy-derived geometric factor, results in exactly twice the value (Collinson et al. 2012, Eq. 11) of the velocity-based definition in Eq. (52). We therefore define the energy-based definition of the geometric factor as:

$$\mathbb{GF} \equiv 2 \cdot \mathcal{GF}. \tag{74}$$

5.4 From Counts to Phase Space Density and Differential Flux

In practice, the geometric factor is used to convert between the count rate measured by the instrument at a specific measurement setting $\mathbf{u}$ and the particle phase space density. Under the assumption that the phase space density of interest does not possess any structure smaller than the instrument response function, we can use Eq. (49), together with the definition of the geometric factor given in Eq. (52) and the simplification laid out in Eq. (54), to obtain the general relation between the count rate and the phase space density at time t:

$$f_\gamma(\mathbf{u}) = \frac{\mathcal{C}_\gamma(\mathbf{u})}{\tau u^4 \eta_\gamma(\mathbf{u}) \mathcal{GF}_0(\mathbf{u})}. \tag{75}$$

Expressing Eq. (75) in the NILS instrument coordinate system and for a given particle species γ of mass m and charge q, we derive the final relation to obtain an evaluation of the particle phase space density, at time t, from all prior knowledge and assumptions laid out in this paper:

$$\boxed{f_\gamma(E_u, \theta_u, \alpha_u) = \left(\frac{m}{2eq\xi_u}\right)^2 \frac{\mathcal{C}_\gamma(\xi_u, \theta_u, \alpha_u)}{\tau\ \eta_\gamma(\xi_u)\ \mathcal{GF}_0(\theta_u)}}. \tag{76}$$

Introducing the definition of the differential number flux

$$J(E_u, \theta_u, \alpha_u)\ [\#/(\mathrm{m}^2.\mathrm{s.sr.J})] \equiv (2E_u/m^2) \cdot f(E_u, \theta_u, \alpha_u),$$

we obtain the following relation:

$$\boxed{J_\gamma(E_u, \theta_u, \alpha_u) = \frac{\mathcal{C}_\gamma(\xi_u, \theta_u, \alpha_u)}{2\tau\ eq\xi_u\ \eta_\gamma(\xi_u)\ \mathcal{GF}_0(\theta_u)}}. \tag{77}$$

5.4.1 Numerical Example

To avoid any misinterpretation of the previously derived equations, we provide a numerical example of a typical counts to physical-units conversion. We assume that for energy bin number 9 and elevation bin number 6, the NILS instrument records a mass spectrum observation with an integration time $\tau = 31.25$ ms.

From the energy Table 2 and the elevation Table 3, we can map the energy and elevation bins to $\xi_u = 1050$ eV/q and $\theta_u = -32$ deg, respectively. However, due to the energy-dependence of the elevation angle as empirically expressed by Eq. (20), at an energy of 1050 eV, the actual elevation angle is: $\theta_u^*(\xi_u = 1050\,\mathrm{eV}) \approx -31$ deg.

From the mass functions given in Sect. 4.6, we can linearly decompose the observed mass spectrum. We assume this process yields a number of 42 counts from H^-.

Table 9 NILS operation modes

Mode name	ID	Purpose
Safe	0	Transient mode during sensor startup
Normal	1	Standby mode, cover opening
EXM	3	Science mode, high voltages on

We therefore see 42 counts attributed to H^- at 1050 eV, arriving from an elevation angle of -31 deg.

The 42 observed counts are derived from the time-of-flight coincidence counter, whose probability of detecting a particle is given in Eq. (48). From Table 7, we can derive that for H^-: $\eta_{coinc}\left(\xi_u = 1050\,\mathrm{eV}\right) \approx 0.014$. The absolute geometric factor, at an elevation angle of -31 deg, is calculated from Eq. (73): $\mathcal{GF}_0\left(\theta_u^* = -31\,\mathrm{deg}\right) \approx 7.84 \times 10^{-5}\left[\mathrm{cm}^2 \cdot \mathrm{sr} \cdot \mathrm{eV/eV}\right]$. We therefore can use Eq. (76) and Eq. (77) to estimate the H^- phase space density and differential number flux as $f_{H^-} \approx 3.02 \times 10^{-22}\left[\mathrm{s}^3 \cdot \mathrm{cm}^{-6}\right]$ and $J_{H^-} \approx 5.83 \times 10^5\left[\#/\left(\mathrm{cm}^2 \cdot \mathrm{s} \cdot \mathrm{sr} \cdot \mathrm{eV}\right)\right]$.

6 Instrument Operation

6.1 Instrument Modes

There are only three distinct operation modes for NILS (Table 9). After power up and executing the low voltage initialisation sequence, NILS is in Normal mode where, for example, configuration updates and cover opening operations can be done. For nominal science operations NILS is put into EXM mode with all high voltages switched on to nominal values.

6.2 Science Mode Measurement Cycle

A complete measurement cycle consists of the acquisition of both an electron and a negative ion energy spectrum for each of the 16 different viewing directions. For each angular viewing direction, NILS acquires an electron and a negative ion energy spectrum by executing the cyclogram shown in Fig. 31. In a first energy sweep, an electron spectrum (e) is acquired with the electron deflection magnet switched off. Only time-of-flight start counters are recorded due to telemetry limitations. This is followed by a second identical energy sweep (i) with the electron deflection magnet switched on. During this second energy sweep, a negative ion mass spectrum together with start and stop counters is recorded. The integration time for each energy step is $\tau = 31.25$ ms. Each of the two energy spectra with 48 energy steps takes 48 $\tau = 1.5$ s to record. There is no additional settling time between individual energy steps. The two energy sweeps are followed by a 1.0 s long sequence where the electron deflector magnet is demagnetised in preparation for the next electron spectrum acquisition. Onboard data processing and compression takes another 60 ms to complete. The remainder of the data acquisition cycle is used to transmit the data to the spacecraft. The time needed for this depends on the rate at which the spacecraft is requesting the data, it typically takes less than 4 s. As soon as there is enough room in the NILS internal data buffer to record a new measurement, the cyclogram shown in Fig. 31 (top) is repeated for the next elevation step until all 16 angular viewing directions have been visited (Fig. 31 bottom). In practice, a complete measurement cycle covering all 16 angular viewing directions plus

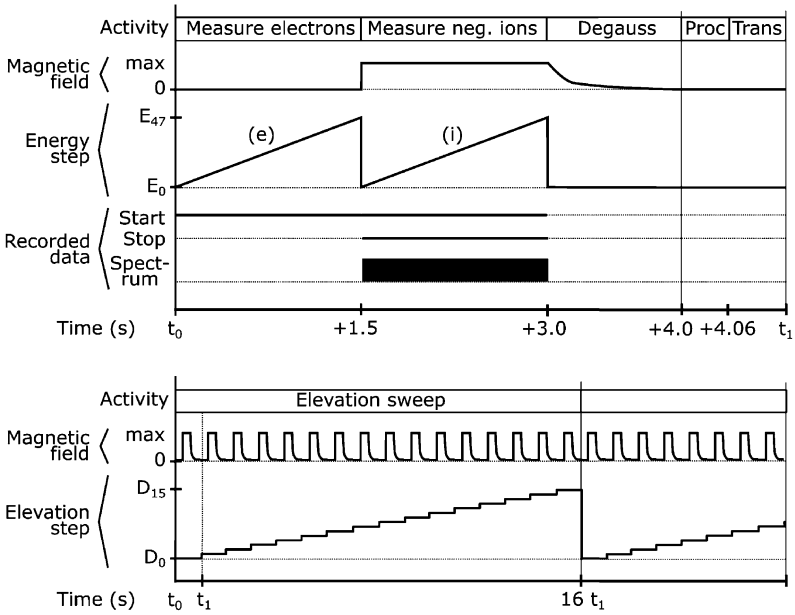

Fig. 31 NILS operation cyclogram. Top panel: Measurement sequence for a single elevation step. During the energy sweep (e) electrons are measured and during the energy sweep (i) the instrument records negative ions. A one second long degaussing sequence for the magnet is followed by 60 ms of data processing and typically one to two seconds of data transmission controlled by the spacecraft data handling unit. Bottom panel: The sequence in the top panel is repeated for each of the 16 elevation steps. The time needed for a complete elevation sweep of $16t_1$ depends on the timing of the data requests from the spacecraft

Table 10 NILS science data structure

Data segment	Content	Sweep	Size (bits)
#0	Header		26×8
#1	48 start counters	(i)	48×16
#2	48 stop counters	(i)	48×16
#3	48 over counters	(i)	48×16
#4	48 start counters	(e)	48×16
#5	48×64 mass bins	(i)	$48 \times 64 \times 16$

the time needed for data transmission takes about 100 s. Different from the implementation in the original SWIM instrument Barabash et al. (2009), the data transmission is entirely controlled by the spacecraft through data polling requests to NILS.

6.3 Data Product

The instrument produces only one type of data product that contains the energy and mass spectra from a single angular pixel. For a complete measurement cycle including 16 elevation steps, 16 such products are produced. The product consists of six segments (Table 10). Segment #0 contains instrument status information and the angular pixel number, segments

Table 11 Standard operation sequence

Time	Commanded	Action
0 s	yes	Power on
	yes	Start producing housekeeping telemetry
10 s	yes	Open protective cover
40 s	yes	Initialise low voltage systems and start producing science telemetry
200 s	yes	Initialise high voltage system
260 s	no	Nominal science configuration reached
t_n	no	Maximum operation temperature exceeded, ramp down high voltages
>3600 s	yes	Shutdown

#1 to #4 various counters from the electron (e) and negative ion (i) energy sweeps, and segment #5 contains the a mass spectrum with 64 elements for each of the 48 energy steps.

To reduce the data volume, all 16 bit elements in segments #1 to #5 are linear-logarithmic encoded to 8 bits (Wieser et al. 2020). For values larger than 63, the encoding is lossy as the least significant bits are discarded, but smaller values are encoded as is. This guarantees that small values can be recovered without losses. For larger values the resulting encoding error is less than 2.5%. After the linear-logarithmic encoding, the segments #1 to #5 are further lossless compressed using a Rice-Golomb scheme (Golomb 1966; Rice et al. 1993).

6.4 Telemetry Handling

The protocol on the command and data interface internally implements the CCSDS (Consultative Committee for Space Data Systems) standard (https://public.ccsds.org). Data packets following the standard are of a variable size. The actual communication with the spacecraft is based on fixed data packet sizes however. To accommodate the variable sized CCSDS packets, the telemetry is buffered internally in NILS until a sufficient number of data bytes are accumulated. Upon a polling request from the spacecraft, a constant sized data packet is then sent. On ground, this stream of fixed sized packets is then reassembled back into the original CCSDS data packets of variable length.

6.5 Standard Operation Sequences

The operation strategy of the NILS instrument is optimised for a lander. The number of telecommands needed is minimised and most functionality is provided by instrument internal macros. The nominal operation sequence is shown in Table 11. After landing the instrument is facing the Sun and it will start to warm up. NILS is then switched on as soon as possible. The instrument cover is opened and science operations start. During operation, the internal temperature continues to increase and will reach an equilibrium after some time. If the internal temperature exceeds the selected maximum operation temperature of the high voltage system, voltages will be ramped down to prevent high voltage discharges and the science taking phase ends–unless the maximum allowable operation temperature is increased through a telecommand. If temperatures do not rise above the selected maximum operation temperature science operations continue until NILS is explicitly switched off.

7 Summary

The Negative Ions at the Lunar Surface (NILS) instrument is a compact negative ion mass analyzer for the Chang'E-6 sample return mission. It is designed to establish the presence of negative ions near the lunar surface and to provide energy spectra for the negative ion flux in an energy range from 3 eV/q to 3 keV/q. The instrument has undergone successful calibration and performance testing and fulfils all design requirements. Chang'E-6 successfully landed on the Moon on 1 June 2024, 22:23 UTC. NILS operated successfully for a total of 346 minutes until the end of the Chang'E-6 surface operations.

Acknowledgements The authors thank Mats André for fruitful discussions about the geometric factor. The calibration data processing pipeline uses `Snakemake` (Mölder et al. 2021).

Author Contribution M. W. is the principal investigator of NILS involved in all aspects. M. W. and R. C.-B. developed, built and calibrated the NILS instrument. M. K. and X.-D. W. managed the NILS project for the Swedish Institute of Space Physics. T. M. was involved in the calibration data analysis. S. B. developed the NILS architecture, defined and initiated the project, and coordinated activities. A. Z., W. W., Q. W. Y. Z. H. D. and H. Z. coordinated activities for NSSC and CNSA. N. M. managed the project for the European Space Agency. V. A., A. E., L. K., S. K., D. U., M. O., J. O., J. P. and D. S. were involved in designing and building NILS.

Funding Information Open access funding provided by Umea University. The Negative Ions on the Lunar Surface (NILS) instrument was developed by the Swedish Institute of Space Physics (IRF) in Kiruna, Sweden, on behalf of the European Space Agency (ESA). It was supported by the ESA grant No. 3-17483/22/NL/DB.

Declarations

Financial interests The authors have no relevant financial or non-financial interests to disclose.

Competing Interests The authors have no competing interests to declare that are relevant to the content of this article.

References

Angelopoulos V (2011) The ARTEMIS mission. Space Sci Rev 165(1):3–25. https://doi.org/10.1007/s11214-010-9687-2

Arnold F, Krankowsky D (1971) Negative ions in the lower ionosphere: a comparison of a model computation and a mass-spectrometric measurement. J Atmos Terr Phys 33(11):1693–1702. https://doi.org/10.1016/0021-9169(71)90217-0

Barabash S, Bhardwaj A, Wieser M, et al (2009) Investigation of the solar wind-Moon interaction onboard Chandrayaan-1 mission with the SARA experiment. Curr Sci 96:526–532

Burch JL, Cravens TE, Llera K, et al (2015) Charge exchange in cometary coma: discovery of H-ions in the solar wind close to comet 67P/Churyumov-Gerasimenko. Geophys Res Lett 42(13):5125–5131. https://doi.org/10.1002/2015GL064504

Canu-Blot R (2024) Negative ions in the plasma environment of the moon: observing small signals related to plasma-surface interaction. Licentiate thesis. IRF/Umeå University. [Chapt 5 and Chapt 7 removed from the digital version]

Chaizy P, Rème H, Sauvaud JA, et al (1991) Negative ions in the coma of comet Halley. Nature 349(6308):393–396. https://doi.org/10.1038/349393a0
Chandrasekhar S, Münch G (1946) The continuous spectrum of the sun and the stars. Astrophys J 104:446. https://doi.org/10.1086/144875
Coates AJ, Crary FJ, Lewis GR, et al (2007) Discovery of heavy negative ions in Titan's ionosphere. Geophys Res Lett 34(22). https://doi.org/10.1029/2007GL030978
Coates AJ, Jones GH, Lewis GR, et al (2010) Negative ions in the Enceladus plume. Icarus 206(2):618–622. https://doi.org/10.1016/j.icarus.2009.07.013
Collinson GA, Dorelli JC, Avanov LA, et al (2012) The geometric factor of electrostatic plasma analyzers: a case study from the fast plasma investigation for the magnetospheric multiscale mission. Rev Sci Instrum 83(3):033303. https://doi.org/10.1063/1.3687021
Desai RT, Taylor SA, Regoli LH, et al (2018) Cassini CAPS identification of pickup ion compositions at Rhea. Geophys Res Lett 45(4):1704–1712. https://doi.org/10.1002/2017GL076588
Desai RT, Zhang Z, Wu X, et al (2021) Photodetachment and test-particle simulation constraints on negative ions in Solar System plasmas. Planet Sci J 2(3):99. https://doi.org/10.3847/PSJ/abf638
Freedman D, Diaconis P (1981) On the histogram as a density estimator:L2 theory. Z Wahrscheinlichkeitstheor Verw Geb 57(4):453–476. https://doi.org/10.1007/BF01025868
Funsten HO, Harper RW, McComas DJ (2005) Absolute detection efficiency of space-based ion mass spectrometers and neutral atom imagers. Rev Sci Instrum 76(5):053301. https://doi.org/10.1063/1.1889465
Golomb S (1966) Run-length encodings (corresp.). IEEE Trans Inf Theory 12(3):399–401
Halekas JS, Lillis RJ, Mitchell DL, et al (2015) Maven observations of solar wind hydrogen deposition in the atmosphere of Mars. Geophys Res Lett 42(21):8901–8909. https://doi.org/10.1002/2015GL064693
Jans S, Wurz P, Schletti R, et al (2001) Negative ion production by surface ionization at barium zirconate surface. Nucl Instrum Methods B 173:503–515. https://doi.org/10.1016/S0168-583X(00)00421-3
Johnstone AD, Coates AJ, Wilken B, et al (1987) The Giotto three-dimensional positive ion analyser. J Phys E, Sci Instrum 20(6):795–805. https://doi.org/10.1088/0022-3735/20/6/038
Kessel RL, Johnstone AD, Coates AJ, et al (1989) Space plasma measurements with ion instruments. Rev Sci Instrum 60(12):3750–3761. https://doi.org/10.1063/1.1141075
Laurence TA, Chromy BA (2010) Efficient maximum likelihood estimator fitting of histograms. Nat Methods 7(5):338–339. https://doi.org/10.1038/nmeth0510-338
Lavraud B, Larson DE (2016) Correcting moments of in situ particle distribution functions for spacecraft electrostatic charging. J Geophys Res Space Phys 121(9):8462–8474. https://doi.org/10.1002/2016ja022591
Lue C, Futaana Y, Barabash S, et al (2011) Strong influence of lunar crustal fields on the solar wind flow. Geophys Res Lett 38(3). https://doi.org/10.1029/2010GL046215
Lue C, Futaana Y, Barabash S, et al (2014) Chandrayaan-1 observations of backscattered solar wind protons from the lunar regolith: dependence on the solar wind speed. J Geophys Res Planets 119(5):968–975. https://doi.org/10.1002/2013JE004582
McComas DJ, Allegrini F, Bochsler P, et al (2009) Lunar backscatter and neutralization of the solar wind: First observations of neutral atoms from the moon. Geophys Res Lett 36(12). https://doi.org/10.1029/2009GL038794
McFadden JP, Carlson CW, Larson D, et al (2008) The THEMIS ESA plasma instrument and in-flight calibration. Space Sci Rev 141(1):277–302. https://doi.org/10.1007/s11214-008-9440-2
Millar TJ, Walsh C, Field TA (2017) Negative ions in space. Chem Rev 117(3):1765–1795. https://doi.org/10.1021/acs.chemrev.6b00480
Mölder F, Jablonski KP, Letcher B, et al (2021) Sustainable data analysis with snakemake. F1000Res 10:33. https://doi.org/10.12688/f1000research.29032.1
Nishino MN, Fujimoto M, Maezawa K, et al (2009) Solar-wind proton access deep into the near-Moon wake. Geophys Res Lett 36(16). https://doi.org/10.1029/2009GL039444
Rice R, Yeh PS, Miller W (1993) Algorithms for high-speed universal noiseless coding. In: 9th computing in aerospace conference. American Institute of Aeronautics and Astronautics. AIAA 1993-4541. https://doi.org/10.2514/6.1993-4541
Saito Y, Yokota S, Tanaka T, et al (2008) Solar wind proton reflection at the lunar surface: Low energy ion measurement by MAP-PACE onboard SELENE (KAGUYA). Geophys Res Lett 35(24). https://doi.org/10.1029/2008GL036077
Schmidt HT, Reinhed P, Orbán A, et al (2012) The lifetime of the helium anion. J Phys Conf Ser 388(1):012006. https://doi.org/10.1088/1742-6596/388/1/012006
Tanaka T, Saito Y, Yokota S, et al (2009) First in situ observation of the Moon-originating ions in the Earth's Magnetosphere by MAP-PACE on SELENE (KAGUYA). Geophys Res Lett 36(22). https://doi.org/10.1029/2009GL040682

Teolis BD, Jones GH, Miles PF, et al (2010) Cassini finds an oxygen–carbon dioxide atmosphere at Saturn's icy moon Rhea. Science 330(6012):1813–1815. https://doi.org/10.1126/science.1198366

Vasyliunas VM (1971) 12. Deep space plasma measurements. In: Methods in experimental physics. Elsevier, Amsterdam, pp 49–88. https://doi.org/10.1016/s0076-695x(08)60859-5

Vorburger A, Wurz P, Barabash S, et al (2014) First direct observation of sputtered lunar oxygen. J Geophys Res Space Phys 119(2):709–722. https://doi.org/10.1002/2013JA019207

Wecker M (2024) Commissioning and characterization of charge conversion particle sources. Master's thesis, Friedrich-Alexander-Universität Erlangen-Nürnberg. https://www.sternwarte.uni-erlangen.de/docs/theses/2024-06_Wecker.pdf

Wekhof A (1981) Negative ions in the ionospheres of planetary bodies without atmospheres. Moon Planets 24(1):45–52. https://doi.org/10.1007/BF00897567

Wieser M, Barabash S (2016) A family for miniature, easily reconfigurable particle sensors for space plasma measurements. J Geophys Res Space Phys 121(12):11,588–11,604. https://doi.org/10.1002/2016JA022799

Wieser M, Wurz P, Bruning K, et al (2002) Scattering of atoms and molecules off a magnesium oxide surface. Nucl Instrum Methods B 192:370–380

Wieser M, Barabash S, Futaana Y, et al (2009) Extremely high reflection of solar wind protons as neutral hydrogen atoms from regolith in space. Planet Space Sci 57(14):2132–2134. https://doi.org/10.1016/j.pss.2009.09.012

Wieser M, Barabash S, Wang XD, et al (2020) The Advanced Small Analyzer for Neutrals (ASAN) on the Chang'E-4 rover Yutu-2. Space Sci Rev 216(4). https://doi.org/10.1007/s11214-020-00691-w

Wieser M, Williamson H, Stenberg Wieser G, et al (2024) Energy spectra of energetic neutral hydrogen backscattered and sputtered from the lunar regolith by the solar wind. Astron Astrophys 684:A146. https://doi.org/10.1051/0004-6361/202348876

Wurz P, Balogh A, Coffey V, et al (2007) Calibration techniques. In: Wüest M, von Evans DS, Steiger R (eds) Calibration of particle instruments in space physics. ISSI scientific reports series, vol SR-007. ESA, Noordwijk, pp 117–276. https://www.issibern.ch/wp-content/uploads/SR-007.pdf

Yokota S, Saito Y, Asamura K, et al (2009) First direct detection of ions originating from the Moon by MAP-PACE IMA onboard SELENE (KAGUYA). Geophys Res Lett 36(11). https://doi.org/10.1029/2009GL038185

Zeng X, Liu D, Chen Y, et al (2023) Landing site of the Chang'e-6 lunar farside sample return mission from the Apollo basin. Nat Astron 7(10):1188–1197. https://doi.org/10.1038/s41550-023-02038-1